

## Simultaneous Multi-Wavelength Observations of Sgr A\* during 2007 April 1-11

F. Yusef-Zadeh<sup>1</sup>, H. Bushouse<sup>2</sup>, M. Wardle<sup>3</sup>, C. Heinke<sup>4</sup>, D. A. Roberts<sup>5</sup>, C.D. Dowell<sup>6</sup>, A. Brunthaler<sup>7</sup>, M. J. Reid<sup>8</sup>, C. L. Martin<sup>9</sup>, D. P. Marrone<sup>10</sup>, D. Porquet<sup>11</sup>, N. Grosso<sup>11</sup>, K. Dodds-Eden<sup>12</sup>, G. C. Bower<sup>13</sup>, H. Wiesenmeyer<sup>14</sup>, A. Miyazaki<sup>15</sup>, S. Pal<sup>15</sup>, S. Gillessen<sup>12</sup>, A. Goldwurm<sup>16</sup>, G. Trap<sup>17</sup>, and H. Maness<sup>13</sup>

### ABSTRACT

We report the detection of variable emission from Sgr A\* in almost all wavelength bands (i.e. centimeter, millimeter, submillimeter, near-IR and X-rays) during a multi-wavelength observing campaign. Three new moderate flares are detected simultaneously in both near-IR and X-ray bands. The ratio of X-ray to near-IR flux in the flares is consistent with inverse Compton scattering of near-IR photons by submillimeter emitting relativistic particles which follow scaling relations obtained from size measurements of Sgr A\*. We also find that the flare statistics in near-IR wavelengths is consistent with the probability of flare emission being inversely proportional to the flux. At millimeter wavelengths, the presence of flare emission at 43 GHz (7mm) using VLBA with milli-arcsecond spatial resolution indicates the first direct evidence that hourly time scale flares are localized within the inner  $30 \times 70$  Schwarzschild radii of Sgr A\*. We also show several cross correlation plots between near-IR, millimeter and submillimeter light curves that collectively demonstrate the presence of time delays between the peaks of emission up to three hours. The evidence for time delays at millimeter and submillimeter wavelengths are consistent with the source of emission being optically thick initially followed by a transition to an optically thin regime. In particular, there is an intriguing correlation between the optically thin near-IR and X-ray flare and optically thick radio flare at 43 GHz that occurred on 2007 April 4. This would be the first evidence of a radio flare emission delayed with respect to the near-IR and X-ray flare emission. The time delay measurements support the expansion of hot self-absorbed synchrotron plasma blob and weaken the hot spot model of flare emission. In addition, a simultaneous fit to 43 and 84 GHz light curves, using an adiabatic expansion model of hot plasma, appears to support a power law rather than a relativistic Maxwellian distribution of particles.

*Subject headings:* accretion, accretion disks — black hole physics — Galaxy: center

## 1. Introduction

The black hole at the center of our own galaxy was first detected as the radio source Sgr A\* over 30 years ago (Balick & Brown 1974). It was found to lie at the center of a cluster of young massive stars. Submillimeter and far-infrared observations showed that Sgr A\* is encircled by a torus of gas approximately 10 light-years across, which orbits with a speed of  $100 \text{ km s}^{-1}$  (e.g. Genzel & Townes 1987). The gravity required to hold onto this material implies a mass of several million solar masses, although a portion of this is contributed by the stars in the stellar cluster. These measurements suggested that Sgr A\* could be a black hole. More detail was provided through studies of the light distribution of stars in the cluster, as well as the motions of ionized and molecular gas clouds orbiting Sgr A\*. These measurements implied a mass of approximately 3–4 million times that of the sun (Genzel 2000; Genzel & Townes 1987) lying within a third of a light year of the radio source. Recently, more precise measurements of fast moving stars in close orbits around Sgr A\* have conclusively demonstrated that it has a mass of  $\sim 4 \times 10^6 M_{\odot}$  (Ghez et al. 2005; Eisenhauer et al. 2005; Ghez et al. 2008; Schödel et al. 2002; Gillessen et al. 2009) and that the size of the radio source is about  $\sim 4$  times its Schwarzschild radius at 230 GHz ( $R_s$ ) (Doeleman et al. 2008). This dark, massive object has also been uniquely identified through the proper motion of the radio source, which show that Sgr A\* must contain  $> 4 \times 10^5 M_{\odot}$  (Reid & Brunthaler 2004). Taken together, these measurements provide strong evidence that Sgr A\* is a black hole with mass  $\sim 4 \times 10^6 M_{\odot}$ . No other known category of astrophysical object can easily fit so much mass into a sub-AU-size region.

This massive black hole is a hundred times closer to us than the next nearest example, presenting an

---

<sup>1</sup>Dept. of Physics and Astronomy, Northwestern University, Evanston, IL 60208,

<sup>2</sup>STScI, 3700 San Martin Drive, Baltimore, MD 21218

<sup>3</sup>Department of Physics and Engineering, Macquarie University, Sydney NSW 2109, Australia

<sup>4</sup>Dept. of Physics, University of Alberta, Room #238 CEB, 11322-89 Avenue, Edmonton AB T6G 2G7, Canada

<sup>5</sup>Adler Planetarium and Astronomy Museum, 1300 South Lake Shore Drive, Chicago, IL 60605

<sup>6</sup>Cal Tech, Jet Propulsion Laboratory, Pasadena, CA 91109

<sup>7</sup>Max-Planck-Institut für Radioastronomie, Auf dem Huegel 69, 53121 Bonn, Germany

<sup>8</sup>Harvard-Smithsonian CfA, 60 Garden Street, Cambridge, MA 02138

<sup>9</sup>Oberlin College, Dept. of Physics and Astronomy, Professor 110 N. St., Oberlin, OH 44074

<sup>10</sup>National Radio Astronomy Observatory; University of Chicago, 5640 South Ellis Avenue, Chicago IL 60637

<sup>11</sup>Observatoire astronomique de Strasbourg, Université de Strasbourg, NRS, INSU, 11 rue de l'Université, 67000 Strasbourg, France

<sup>12</sup>Max-Planck-Institut für Extraterrestrische Physik 1312, D-85471, Garching, Germany

<sup>13</sup>Radio Astronomy Lab, 601 Campbell Hall, University of California, Berkeley, CA 94720

<sup>14</sup>Institut de RadioAstronomie Millimetrique, 300 rue de la Piscine, Domaine Universitaire 38406 Saint Martin d'Herès, France, on leave to IRAM Granada, Spain

<sup>15</sup>Mizusawa VLBI Observatory, National Astronomical Observatory of Japan, Mizusawa, Oshu, Iwate 023-0861, Japan

<sup>16</sup>Service d'Astrophysique / IRFU / DSM, CEA Saclay, Bat. 709, 91191, Gif-sur-Yvette Cedex, France and AstroParticule & Cosmologie (APC) / Université Paris VII / CNRS / CEA / Observatoire de Paris Bat. Condorcet, 10, rue Alice Domon et Léonie Duquet, 75205 Paris Cedex 13, France

unparalleled opportunity to closely study the process by which gas is captured by black holes. It is therefore the subject of intense scrutiny. The energy radiated by Sgr A\* is thought to be liberated from gas that is falling into the black hole after being captured from the powerful winds of members of its neighboring cluster of massive stars (e.g., Melia 1992). The broad band spectrum of Sgr A\* peaks at submillimeter wavelengths (Zylka et al. 1992; Falcke et al. 1998); this is thought to be the dividing line between optically thick and optically thin emission at low and high frequencies, respectively. The bolometric luminosity of Sgr A\*  $\sim 100 L_{\odot}$  is several orders of magnitudes below that predicted given its expected rate of capture of material from stellar winds, prompting a number of theoretical models to explain its very low efficiency (Melia & Falcke 2001; Liu & Melia 2001; Yuan et al. 2003; Goldston et al. 2005; Liu et al. 2004; Falcke et al. 2009).

Now that the quiescent spectrum of emission from Sgr A\* has been characterized from radio to X-rays, attention has turned to variability of emission in multiple wavelengths. These measurements probe the structure and the physical parameters of the hot plasma in the vicinity of the black hole by measuring the time variations of its flux in different wavelength bands as well as their cross-correlation with each other. Flaring activity on  $< 1 - 4$  hour time scale is seen in all wavelength bands in which quiescent emission has been detected.

Flaring X-ray emission from Sgr A\* has been detected and has been argued to originate within a few Schwarzschild radii of the  $\sim 4 \times 10^6 M_{\odot}$  black hole (Baganoff et al. 2003; Goldwurm et al. 2003; Porquet et al. 2003; Bélanger et al. 2005). At near-IR (NIR) wavelengths (Genzel et al. 2003; Yuan et al. 2003; Ghez et al. 2004; Hornstein et al. 2007), flare emission from Sgr A\* is shown to be due to optically thin synchrotron emission, whereas the long-wavelength flaring activity in submillimeter, millimeter and centimeter bands is due to optically thick synchrotron emission. The exact frequency at which the transition from optically thick to thin flare emission occurs is unknown.

A variety of mechanisms have been proposed to explain the origin of the variability of Sgr A\*. Many of these models have considered different energy distributions for the relativistic particles to explain the origin of submillimeter emission (Melia & Falcke 2001; Yuan et al. 2002; Melia 2002; Liu & Melia 2002; Yuan et al. 2003; Eckart et al. 2004, 2006a,b; Gillessen et al. 2006; Goldston et al. 2005; Liu et al. 2006). The direction that has been taken in the past in interpreting the flaring activity of Sgr A\* is within one of the established paradigms for the accretion flow that have been developed based on the time-averaged emission. Typically one or another paradigm for the flow is adopted – for example a thin accretion disk, a disk and jet, outflow, an advection-dominated accretion flow, radiatively inefficient accretion flow, accretion disk inflow/outflow solutions (Melia 1992; Yuan et al. 2003; Falcke & Markoff 2000; Falcke et al. 2009; Narayan et al. 1998; Blandford & Begelman 1999) and then the predicted spectrum is compared with the observed spectrum. One has little choice to follow this “top-down” approach for the mean emission, as this is produced by the entire flow of gas falling into the hole. The weakness of this approach is twofold. First, the adoption of a particular *a priori* model naturally leads to a tendency to push hard to fit theoretical predictions to the observations. Second, the entire accretion flow has to be calculated from large distances down to the event horizon. This necessity means adopting prescriptions to cover gaps in our knowledge of fundamental aspects of astrophysical fluid dynamics, such as angular momentum transport, magnetic reconnection, and particle acceleration.

What has not been fully appreciated is that focusing on the variability of the emission rather than the underlying constant component frees us from the need to model the entire flow into the hole because this emission comes from *localized* hot regions. Thus, one can instead compute a

relatively simple model of the temporarily bright region, recovering the physical conditions in a way that is paradigm-independent. This allows an “observations up” approach that treats each flare as a sample of the accretion flow or an outflow. A similar approach has recently been taken by Loeb & Waxman (2007) who suggest an outflow from Sgr A\* by inferring first the scaling of the temperature, electron density, and the magnetic field strength using the observed spectrum and wavelength-dependent angular size of Sgr A\* (similar constraints are used in the inverse Compton picture, as described in section 4.4). Then, they argue that an increase in the electron temperature above the virial temperature at about tens of  $R_g$  will result unbound plasma.

We have recently used this “observations up” approach to analyze the NIR flaring of Sgr A\*, which is produced by synchrotron emission from a transient population of particles produced within  $\sim 10$  Schwarzschild radii of the massive black hole (Genzel et al. 2003; Eckart et al. 2006a; Gillessen et al. 2006). We argued that the  $\sim 2 - 3$  hour duration of submillimeter flares could not be due to synchrotron cooling when observed simultaneously with a NIR flare (estimated to be  $\sim 20$  minutes and  $\sim 12$  hours at  $1.6\mu\text{m}$  [188 THz] and  $850\mu\text{m}$  [350 GHz], respectively). The decline in submillimeter light curves was interpreted to be due to adiabatic cooling associated with expansion of the emitting plasma (Yusef-Zadeh et al. 2006a,b) under the assumption that the same accelerated population of particles is responsible for NIR and submillimeter emission. Time delays detected between peaks of flare emission at radio, submillimeter and NIR/X-rays wavelengths are consistent with this picture (e.g., Marrone et al. 2008; Yusef-Zadeh et al. 2008; Meyer et al. 2008; Eckart et al. 2008). However, the lack of long simultaneous coverage have not placed strong constraints in time delay measurements, especially between radio and NIR wavelengths. Simple modeling of the total and polarized intensity of the hot expanding plasma provide predictions that can be tested observationally by carrying out observational campaigns such as the one we coordinated during April 2007 to examine the mechanisms for the variability, with implications on the nature of the accretion flow. The results presented here are the third in a series of papers that came from this multi-wavelength observing campaign (Porquet et al. 2008; Dodds-Eden et al. 2009). The results of soft  $\gamma$ -ray observations are given separately (Trap et al. 2009).

The structure of this paper is as follows. §3 presents light curves of all the useful data that were taken in this campaign, following the observational details described in §2. In §4 we analyze the statistical properties of flare emission and the corresponding spectral and power spectrum distributions at NIR wavelengths, as well as cross-correlation analysis of light curves. We then discuss in §5 the origin of X-ray emitting flares and provide observational support for the expanding hot plasma model of flare emission. The polarization results will be given elsewhere.

## 2. Observations and Data Reduction

The primary purpose of observations made during 2007 April 1-11 was the coordination of several telescopes operating at many wavelengths to monitor the emission from Sgr A\* and measure the time evolution of its spectrum. There were a total of 13 observatories that participated in this campaign, including XMM-Newton, the Hubble Space Telescope (HST), the International Gamma-Ray Astrophysics Laboratory INTEGRAL, the Very Large Array (VLA) of the National Radio Astronomy Observatory<sup>17</sup> (NRAO), the Very Long Baseline Array (VLBA<sup>17</sup>), the Caltech Submillimeter

---

<sup>17</sup>The National Radio Astronomy Observatory is a facility of the National Science Foundation, operated under a cooperative agreement by Associated Universities, Inc.

Observatory (CSO), the Very Large Telescope (VLT), the Submillimeter Array (Blundell 2004), the 30m Pico Veleta Telescope of the Institute for Millimeter Radioastronomy (IRAM), the Submillimeter Telescope (SMT), the Nobeyama Millimeter Array (NMA), the Combined Array for Research in Millimeter-wave Astronomy (CARMA), and the Giant Meterwave Radio Telescope (GMRT). The campaign was organized by first obtaining observing time with XMM-Newton (PI: D. Porquet) and HST (PI: F. Yusef-Zadeh), and then coordinating the ground-based facilities to the allotted space-based schedules.

Figure 1 shows the schedule of all observations and their rough durations. Details of XMM-Newton and VLT/NACO observations have already been reported in Porquet et al. (2008), and (Dodds-Eden et al. 2009), respectively. Summary of the results from VLT/VISIR and INTEGRAL observations has also been given by Trap et al. (2009). Briefly, XMM observations were carried out using three observations for a total of 230 ks blocks of time during 2007 March 30 to April 4, and the VLT/NACO observations took place between 2007 April 1–6 using H ( $1.66\ \mu\text{m}$ ), K ( $2.12\ \mu\text{m}$ ), and L' ( $3.8\ \mu\text{m}$ ) bands. INTEGRAL observations took place in parallel to XMM-Newton on April 1 and 4 for a total effective exposure time of 212 ks for IBIS/ISGRI (20–100 keV) and 46 ks for JEM-X 1 (3–20 keV).

### 2.1. HST NICMOS: $1.45\ \mu\text{m}$ and $1.70\ \mu\text{m}$

We obtained 40 orbits of HST observations using the NICMOS camera 1, with the orbits distributed over seven consecutive days between 2007 April 1–7. The observations used the NICMOS F145M and F170M filters, with exposure times of 144 sec in each filter and readout samplings of  $\sim 16$  sec within each exposure. Use of this pair of filters has several advantages. First, they have no overlap in wavelength space and are therefore suitable for spectral index measurements. Second, they are well matched to one another in terms of throughput, so that we can use identical exposure and readout times, thus producing time series data that are evenly sampled in both filters. This has great advantages for making periodicity measurements. Third, their relatively high throughput also allows us to use relatively short exposure times, so that we can cycle back and forth between the two filters fairly rapidly. The near-simultaneous observations then allow us to make meaningful spectral index measurements of flare events. This is especially true for the peaks of flare events, where the flux from Sgr A\* does not change rapidly over the course of several minutes or more. The spectral index distribution can not be measured accurately, however, during the rise and fall of flare events because the overall flux is changing more rapidly than the cadence of our filter cycling times.

The IRAF “apphot” routines were used to perform aperture photometry of sources in the NICMOS Sgr A\* field, including Sgr A\* itself. For stellar sources the measurement aperture was positioned on each source using an automatic centroiding routine. This approach could not be used for measuring Sgr A\* because its signal is spatially overlapped by that of the orbiting star S0-2 and S17. Therefore the photometry aperture for Sgr A\* was positioned by using a constant offset from the measured location of S0-2 in each image. The offset between S0-2 and Sgr A\* was derived from the orbital parameters given by Ghez et al. (2003). The position of Sgr A\* was estimated to be  $0.16''$  south and  $0.01''$  west of S0-2 at the time of the HST observations. To confirm the accuracy of the position of Sgr A\*, two images of Sgr A\* taken before and during a flare event were aligned and subtracted, which resulted in an image showing the location of the flare emission.

We used a measurement aperture with a diameter of 3 detector pixels, which corresponds to  $\sim 0.13''$ .

This size was chosen as a suitable compromise between wanting to maximize the fraction of the Sgr A\* PSF included in the aperture, while at the same time limiting the amount of signal coming from the wings of the PSF from the adjacent star S0-2. We derived aperture correction factors by making measurements of a reasonably well isolated star in the field through a series of apertures of increasing size. The aperture corrections, which convert the fluxes measured through our 3-pixel diameter aperture to a semi-infinite aperture, are 2.91 and 3.40 for the 1.45 and 1.70  $\mu\text{m}$  bands, respectively. Absolute calibration of the photometric measurements was accomplished using the latest calibrations for the NICMOS F145M and F170M obtained from STScI.

De-reddened fluxes were computed using the appropriate extinction law for the Galactic center (Moneti et al. 2001) and their extinction value of  $A(K)=3.3$  mag. These translate to extinction values for the NICMOS filter bands of  $A(F170M)=5.03$  mag and  $A(F145M)=6.52$  mag, which then correspond to correction factors of 103 and 406, respectively. Because there is some contribution from the neighboring star S0-2 within our measurement aperture, we have determined the flux of Sgr A\* when it is flaring by subtracting the mean flux level measured during “quiescent” episodes. The resulting net flux can therefore be safely attributed to Sgr A\* flares.

## 2.2. VLA: 43 and 22 GHz

We used a fast-switching technique to observe Sgr A\* simultaneously using the VLA D configuration at 43.3 GHz (7mm) and 22.4 GHz (13mm) GHz. These observations took place on 2007 April 1–4, each lasting for  $\sim 7$  hours, using 8 VLA and 18 eVLA antennas. The two IFs were separated by 50MHz in each observation, except for those on 2007 April 4, when the two IFs were centered at non-standard frequencies of 43.1851 and 43.5351 GHz, which corresponds to a frequency separation of 350 MHz. The separation was used to carry out polarization measurements, the result of which will be given elsewhere.

We cycled between Sgr A\* and the fast-switching calibrator 17444-31166 (2.3 degrees away from Sgr A\*) for 90 sec and 30 sec, respectively, throughout the observation. On 2007 April 4, we also used the fast-switching phase calibrator 17459-28204, which is weaker, but closer ( $\sim 21'$ ) to Sgr A\*. 3C286 was used as the flux calibrator and NRAO530 was observed as a polarization and additional phase calibrator. The light curves at 43 GHz restricted data to a  $uv$  range greater than 90 k $\lambda$  with full width at half point of  $2.45'' \times 1.3''$  ( $PA=-4^\circ$ ). We used NRAO530 for pointing every 30 minutes; the bootstrapped flux of NRAO530 at 43 GHz is  $2.43 \pm 0.05$  Jy. At 22 GHz, the strong continuum emission from ionized gas associated with extended features surrounding Sgr A\* overwhelmed the flux of Sgr A\* itself, making the variability analysis uncertain. Therefore the 22 GHz data are not useful and are not presented here. In all the measurements presented here, we used only antennas that had constant gain curves with similar values, thus many of the eVLA antennas were not used.

In all cases, at least two and sometimes three phase calibrators were used in order to ensure that amplitude variability or calibration errors of one of the calibrators would not be introduced into the light curve of Sgr A\*. In the case of multiple phase calibrators, the same calibrator used to calibrate the gains of Sgr A\* was used to cross-calibrate the other calibrators. In cases where calibrator light curves are shown as alongside those of Sgr A\*, they were obtained from cross-calibration using one of the other phase calibrators and *not* from self-calibration. Additionally, as a check, all light curves of Sgr A\* made using phase calibrations from the principle phase calibrator (usually 17444-31166) were compared against light curves of Sgr A\* made using the other phase calibrators. These comparisons were used to identify bad data in the calibrators and after editing and recalibration

light curves using different calibrators were consistent.

For the final light curves of Sgr A\*, the data were calibrated using the principle phase calibrator (17444-31166). A phase self-calibration was applied to Sgr A\* before the determination of a light curve. No amplitude self-calibration was done to Sgr A\* or any backup phase calibrators, whose light curves are shown as a reference, since amplitude calibration would remove time variation from the light curves. After phase self-calibration, large images were made and found no confusing point sources above the rms noise (typically  $2.5 \text{ mJy beam}^{-1}$  in a full run at 43 GHz) when the selected uv data were greater than  $90k\lambda$ .

In order to derive the light curve in the visibility plane, the Astronomical Image Processing System (AIPS) task DFTPL was used. DFTPL plots the direct Fourier transform of a vector averaged set of measured visibilities as a function of time. Since we use this on data that has been phase self-calibrated using the point source Sgr A\*, the vector average gives the flux of Sgr A\*. Visibilities are averaged in bins with defined time widths, however, since the number of visibilities in each bin varies, the error associated with the average will not be constant and are derived at each time range.

### 2.3. VLBA: 43, 22, and 15 GHz

We observed Sgr A\* with the VLBA in two different experiments. One took place on 2007 April 1, 5 and 11 at 43 GHz under program BR124. All observations employed four 8 MHz bands in dual circular polarization each. These observations were made at 43 GHz and involved rapid switching between Sgr A\* and the two background continuum sources J1748-291 and J1745-283. Sources were changed every 15 seconds in the sequence Sgr A\* – J1748-291 – Sgr A\* – J1745-283 – Sgr A\*, yielding an on-source time of  $\sim 10$  seconds. Before, in the middle, and after each observation 16 quasars were observed within  $\sim 40$  minutes. NRAO 530 was also observed as fringe-finder. The total observing time including the quasars was 8 hours for each observation. The data were correlated with 16 spectral channels per frequency band and an integration time of 0.131 seconds. The  $\sim 1$  hour gaps in the light curves of Sgr A\* are due to geodetic measurements.

In the second experiment (proposal code BB230), the observations on 2007 April 2 and 10 involved rapid switching between two frequencies on Sgr A\*. We observed 43 and 22 GHz on 2007 April 2 and 43 and 14 GHz on April 10. We changed the receiver every 20 seconds, yielding an on-source time of  $\sim 10$  seconds for each frequency. The observations were interrupted three times by 20 minute observations of four different quasars, including the fringe-finder 3C 345. All data were correlated with 16 spectral channels per band and an integration time of one second. The total observing time including the quasars was 6 hours for each observation.

The VLBI data were edited and calibrated using standard techniques in AIPS. First, we applied the latest values of the Earth’s orientation parameters. A-priori amplitude calibration was applied using system temperature measurements and standard gain curves. We performed a “manual phase-calibration” using the data from NRAO 530 or 3C 345 to remove instrumental phase offsets among the three frequency bands. Then, we fringe fitted the data from Sgr A\* using only the five inner VLBA antennas (PT, KP, FD, OV, and LA). Then, we discarded all data with elevations below  $15^\circ$  and performed one round of phase self-calibration on Sgr A\*. Finally, we divided the calibrated uv-data by a model described in Bower et al. (2004), i.e. an elliptical Gaussian component of  $0.71 \times 0.41 \text{ mas}$  with a position angle of  $78^\circ$ . Lightcurves were extracted from the uv-data with the

AIPS task DFTPL.

#### 2.4. CSO: 350 $\mu$ m, 450 $\mu$ m & 850 $\mu$ m

Nightly observations of Sgr A\* were made at three wavelengths over the period 2007 April 1–6 UT, using the SHARC-II camera. The observations on April 1–5 were made with the SHARP imaging polarimeter module installed (Li et al. 2008), using the 350  $\mu$ m half-wave plate. The observing bands (selected by a cryogenic filter) were 450  $\mu$ m on April 1–3 and 350  $\mu$ m on April 4–5. The observations on April 6 were made at 850  $\mu$ m with SHARP removed from the optical path.

In this paper, we report only the total intensity measurements. Because SHARP is a dual-polarization instrument, and because the observations were made over cycles of half-wave plate angles that fully modulate the polarization, our total intensity results are insensitive to the polarization of the source.

Except for the stepping of the polarimeter half-wave plate between integrations, the observing and analysis method was similar to past CSO observations (Yusef-Zadeh et al. 2006a, 2008). We used Lissajous scans with typical full amplitudes of 100'' in both azimuth and elevation. The instantaneous field of view is 57''  $\times$  57'' in polarimeter mode and is 154''  $\times$  58'' without the polarimeter.

The measured beam sizes were 8.4'' at 350  $\mu$ m, 10.1'' at 450  $\mu$ m, and 18.8'' at 850  $\mu$ m. We used the Dish Surface Optimization System (DSOS) on April 1–5. Three quadrants were working fully during the run, but the fourth quadrant of the system was available for only part of the run. For observations at the elevation of Sgr A\*, we expect no significant effect on the results from the non-operational quadrant. Any change in the beam FWHM due to the status of the DSOS quadrant was less than 3%.

Mauna Kea weather conditions were good overall during the April 1–6 campaign. Occasional thin cirrus was observed visually and on satellite photos on April 3, 4, and 6; otherwise skies were clear. Local humidity was < 30% during the observations. The wind speed for April 1 was noticeably high (roughly 30 mph), but less than 20 mph on the other nights. The zenith atmospheric opacity at 225 GHz was marginal for observations at 450  $\mu$ m on April 1 ( $\tau_{225} \approx 0.07$ ), as well as at 850  $\mu$ m on April 6 ( $\tau_{225} \approx 0.15$ ), and rising in both cases. Atmospheric opacity on April 2–5 was excellent and relatively steady, ranging from 0.03 to 0.06 at 225 GHz.

In producing the light curves for this paper, we reconsidered the image registration and absolute calibration for all of our CSO observations of Sgr A\* from 2004 September through 2008 May. The absolute pointing of the images is based on hourly measurements of point-like calibration sources, such as planets, and the pointing model for the telescope. This procedure appears to average down in a reasonable manner. The 350  $\mu$ m and 450  $\mu$ m position that we measure for the variable component of Sgr A\* is within 0.3'' of the nominal position of  $\alpha_{2000} = 17^h : 45^m : 40^s.03$ ,  $\delta_{2000} = -29^\circ : 00' : 28''.1$ . The agreement at 850  $\mu$ m, at which the telescope beam size is larger, is somewhat worse at 0.9''.

At any particular point in time, the telescope pointing model has only  $\sim 2''$  accuracy. Therefore, we shifted the individual observations to align with the average of all the observations, using the bright dust emission in the images as the reference. Subsequent photometry of Sgr A\* assumes a fixed position and beam size.

Minor changes have been made to the absolute calibration scale factor and Sgr A\* “zero point”, in-



cluding data which have been published in the past (Yusef-Zadeh et al. 2006a, 2008; Marrone et al. 2008). For the scale factor, we have adopted the following brightness temperatures for calibration at 350, 450, and 850  $\mu\text{m}$ , respectively: Callisto (128, 122, 120 K), Neptune (61, 66, 81 K), and Uranus (64, 70, 86 K), arranged in decreasing order of usage and with an estimated 10% uncertainty. These brightness temperatures are not significantly different from our past assumptions. The zero point relates to the difficulty of measuring the total flux of Sgr A\* with  $\sim 10''$  resolution because of confusion from surrounding dust emission. We estimate an additive uncertainty of 1 Jy in our measurements of the absolute flux at 350  $\mu\text{m}$  and 850  $\mu\text{m}$ , and an additive uncertainty of 0.5 Jy at 450  $\mu\text{m}$ . To be consistent with the results published in this paper, the August–September 2004 measurements at 850  $\mu\text{m}$  reported by Yusef-Zadeh et al. (2006a) should be shifted upwards by  $\sim 0.2$  Jy; the 450  $\mu\text{m}$  measurements for the same period are essentially unchanged. The 850  $\mu\text{m}$  measurements for July 2006, reported by Yusef-Zadeh et al. (2008) and (Marrone et al. 2008), should be shifted upwards by  $\sim 0.5$  Jy. The 350  $\mu\text{m}$  results for July 2005, reported by (Marrone et al. 2008), should be shifted upwards by  $\sim 0.4$  Jy; the 450  $\mu\text{m}$  and 850  $\mu\text{m}$  results for the same period are essentially unchanged.

## 2.5. SMA: 230 GHz

The SMA observed Sgr A\* on the nights of 1, 3, 4, and 5 April 2007, typically covering the interval 1200–1830 UT. On the first three nights the array was tuned to observe 231.9 (221.9) GHz in the upper (lower) sideband, while on the last night the frequency was tuned to 246.0 (241.0) GHz. The array was in its “compact-north” configuration, resulting in angular resolution of approximately  $3''$ . All eight antennas were used except on April 4, when one was lost to an instrument problem. The SMA polarimetry system (Marrone & Rao 2008) was used in these observations to convert the linearly polarized SMA feeds to circular polarization sensitivity, which prevents confusion between linear polarization and total intensity variations.

The data were gain calibrated using the quasar J1733–130, which was observed approximately every 10 minutes. The absolute flux density scale was derived from observations of Callisto and has an uncertainty of 10%. To remove the effects of the extended emission that surrounds Sgr A\*, only projected baselines longer than 20 k $\lambda$  were used in the light curve determination. Flux density measurements were made by applying the quasar gains to the Sgr A\* data, removing the average phase on Sgr A\* in each light curve interval via phase self-calibration, which reduces the effect of baseline errors and phase drifts on the measurement, and fitting a central point source to the calibrated visibilities. Errors in the flux density account for thermal noise, as well as the time-variable uncertainty in the gain, which is estimated from the data themselves.

## 2.6. IRAM-30m Telescope: 230 GHz

Observations with the IRAM-30m telescope at Pico Veleta, Spain, were carried out on 2007 April 1–4. Because of the low elevation of Sgr A\* at Pico Veleta, gain drifts due to atmospheric fluctuations are the most severe limitation to accurate flux monitoring. For the same reason, accurate peak-up is important if flux variations are to be measured that are small with respect to the quiescent flux. To account for both requirements, we alternated between Sgr B2 and Sgr A\* with the following procedure, applying a wobbling secondary mirror to remove the 230 GHz emission from the atmospheric and from extended ( $> 70''$ ) source structure. First, we pointed at Sgr B2 and

measured the position of its point-source component by fitting simultaneously a Gaussian and a linear baseline (for a refined removal of extended emission) to the pointing subscans taken in on-the-fly mode (two in azimuth direction, two in elevation). The positional correction was entered and the procedure repeated to recover the correct flux. We used either the azimuth or elevation subscan, depending on where the flux was larger (and thus a better peak-up was provided). Then the antenna was moved to Sgr A\*, where the same procedure was repeated. Thus, for each time sample, there are two data points representing the flux of Sgr A\*, one from the pointing, and another one from the peaked up pointing. Both results were used if the pointing correction was sufficiently small. Error estimates were made by comparing the results of subscans in the same direction. To avoid effects due to instrumental and atmospheric gains drifts, only scaled fluxes of Sgr A\* were retained for further analysis, using Sgr B2 as a non-variable flux reference. Data reduction was done with the MOPSIC software package <sup>18</sup> The average Sgr B2 flux density is estimated to be  $38.0 \pm 1.2$  Jy and was derived using the HII region G10.62-0.38 as absolute flux reference. The beam FWHM is  $11''$ .

## 2.7. SMT: 250 GHz

Observations were undertaken at the SMT located at 3200m altitude on Mount Graham in eastern Arizona Baars et al. (1999) using the 250 GHz channel of the facility’s four color bolometer Kreysa (1990). This bolometer was used to observe at 250 GHz with a broad band, ranging between 200 and 290 GHz on 2007 April 1–4. We made use of the telescope’s beam switching mode, chopping horizontally  $\pm 2'$  with the subreflector at a rate of 2 Hz along with an “off-on-on-off” observing mode that shifted the position of the telescope every 10 seconds to remove any asymmetries in the observations due to the chopping. Jupiter, Saturn, and Mars were used for focus and pointing references confirming the telescope’s typical half power beam width at these frequencies of  $30''$  and pointing accuracy of  $2''$ . While Jupiter was used to set the gain of the bolometer and skydips to find the atmospheric opacity, NRAO 530, 1757-240 and G34.3 were also observed throughout the observations as secondary calibrators to check the stability and repeatability of the measurements. Finally, after splitting the data into 80 second increments (consisting of two iterations of the 40 second long “off-on-on-off” observing mode), the raw data were reduced using a version of the standard GILDAS NIC reduction program customized for the four color bolometer. Because a single calibrator was not used continuously during the first two days of observations, the flux variation of Sgr A\* was uncertain and thus the data are not presented here.

## 2.8. NMA: 150 & 230 GHz

Interferometric NMA observations were carried out simultaneously at 90 and 102 GHz in the 3-mm band, and simultaneously at 134 and 146 GHz in the 2-mm band with bandwidth of 1024 MHz on 2007 April 1–4. The 2 and 3 mm flux densities are measured to be  $1.8 \pm 0.4$  and  $2.0 \pm 0.3$  Jy, respectively. The light curves of data from April 3 and 4 are presented using five and six antennas, respectively. The weather was bad on April 1 and 2 so we discarded the data on the first days of observations. 1744-31 (J2000) was used as the phase calibrator and the data was binned every 3-4 minutes. The flux measurements of Sgr A\* were estimated by fitting a point source model in the

---

<sup>18</sup><http://www.iram.es/IRAMES/mainWiki/CookbookMopsic>

$uv$  plane restricted to distances  $> 20$  k $\lambda$ , in order to suppress the contamination from extended components surrounding Sgr A\*. The FWHM of the synthesized beam in the 2mm observation on 2007, April 4 is  $6'' \times 1.4''$ . We used 3C279 as a passband calibrator and Neptune as the primary flux calibrator.

## 2.9. CARMA: 94 GHz

Interferometric CARMA observations were done to observe Sgr A\* on 2007, April 2-5. Observations were made at 94 GHz using nine 6m diameter BIMA and six 10m diameter OVRO antennas with the exception of observations on 2007, April 3 which did not include any OVRO antennas. In all days, Uranus was used as the primary flux calibrator, 1744-312 as the complex gain calibrator and 1751+096 was used as a passband calibrator. The weather was poor for observing at 94 GHz on the first half of 2007, April 3 and the second half of 2007 April 4. We did not include the data during these times. Five frequency windows, each 469 MHz wide, were used at frequencies from 94 to 100 GHz. We used NRAO530 (1730-130) to cross calibrate 1744-312, in order to independently track the amplitude stability of 1744-312. All calibration was done using MIRIAD package and calibrated visibility data for each day were read into AIPS and the DFTPL task was used to extract light curves for the source.

## 2.10. GMRT: 1.28 GHz

We observed Sgr A\* using Giant Meterwave Radio Telescope (GMRT) in 1280, 610 and 325 MHz frequencies with central observation time on MJD 54195.0, 54191.1 and 54190.1 (5.0 April, 1.1 April and 31.1 March 2007 UT) respectively. GMRT<sup>19</sup> consists of thirty fully steerable parabolic antenna array, where fourteen antennas are randomly distributed in 1 km area and rest of the sixteen antennas are placed in three arms, spread over 25 km area, forming nearly a shape like ‘Y’. The diameter of each antenna is forty five meter. Observation band-width in each frequency was 32 MHz and integration time was 16.9 second. The source was observed for 6.1, 4.2 and 7.0 hr in 1280, 610 and 325 MHz respectively. We have done flux calibration using 3C286 and 3C48 and used Baars et al. (1977) for setting flux density scale. J1830-360 was used as phase calibrator. The bad data and radio frequency interferences (RFIs) are eliminated from the data set and the source is self-calibrated. The original data has channel width of 125 KHz in the spectral line mode. To take care of effect of the band width smearing in low frequency, we did not averaged all the channels after calibration but averaged 32, 16 and 8 channels in 1280, 610 and 325 MHz respectively (forming effective channel width of 4, 2 and 1 MHz in 1280, 610 and 325 MHz). The images are corrected for the beam-shape. Because of the strong emission from the nonthermal emission surrounding Sgr A\*, the light curve of Sgr A\* could have not been obtained reliably at 330 and 630 MHz. This is mainly due to the instantaneous elongated beam shape which contains extended structures surrounding Sgr A\*. For this reason, we only present the 1.28 GHz light curve and restrict the  $uv$  data to  $> 80$ k $\lambda$ .

---

<sup>19</sup>[www.gmrt.ncra.tifr.res.in](http://www.gmrt.ncra.tifr.res.in)

### 3. Light Curves: Individual Telescopes

The results of XMM and VLT observations in X-ray and NIR have already been presented elsewhere (Porquet et al. 2008; Dodds-Eden et al. 2009). A detailed account of INTEGRAL observations are given elsewhere (Trap et al. 2009). To present all the data that were taken during this campaign, we include the XMM and VLT light curves again here and briefly review the results of these observations that have already been published elsewhere.

#### 3.1. NICMOS Photometric Measurements

Figure 2a shows the observed variability of Sgr A\* in the NICMOS 1.45 and 1.70 $\mu$ m bands, where there is good agreement between the two bands. The observed “quiescent” emission levels of Sgr A\* in the 1.45 and 1.70 $\mu$ m bands are  $\sim 32$  and  $\sim 38.5$  mJy, respectively, but some fraction of this total signal is due to the neighboring star S0-2. During flare events, the emission is seen to increase by anywhere from a few percent to 25% above these levels. In spite of the somewhat lower signal-to-noise ratio for the 1.45 $\mu$ m data, due to the somewhat lower sensitivity of the NICMOS detector and increased effects of extinction, the flare activity is still easily detected in this band. In order to confirm that the observed variability of Sgr A\* is not due to either instrumental or data reduction effects, we have compared the Sgr A\* light curves to that of the star S0-2 and to a region of background emission with the NICMOS images, as shown in Figure 2b. The photometric measurements for Sgr A\* show obvious signs of variability in six of the days of HST observations, while the corresponding light curves of S0-2 and the background remain quite stable.

The panels of Figure 3 present detailed light curves of Sgr A\* and, for comparison, S0-2 for each of the seven HST observing windows. These plots show the time-ordered measurements in the 1.45 and 1.70 $\mu$ m bands, where we have now subtracted the mean “quiescent” flux level, leaving the net variations in emission for both Sgr A\* and S0-2. All light curves are aperture and extinction corrected. Each observing window consists of 5 to 7 HST orbits, with each orbit covering  $\sim 46$  minutes. We have identified flaring activity in at least one orbit in each of the seven observing windows. These activities are identified in the light curves with labels designating the day (1–7) and the flare even within the day (A–C). A typical flare event lasts between 10 and 40 minutes. The amplitudes and durations of the events are similar to what was found in our earlier HST observations (Yusef-Zadeh et al. 2006a). These new measurements, however, show the appearance of minute-time scale intensity fluctuations that had not been realized in our previous HST observations.

To examine the short time scale variability in more detail, the 1.70 $\mu$ m light curves are shown in Figure 4 with a sampling of 64 seconds. The Sgr A\* and S0-2 light curves are qualitatively similar to those in Figure 3, except for the finer sampling and we show only the 1.70 $\mu$ m band because the 1.45 $\mu$ m data do not have sufficient signal-to-noise in this shorter integration period. There are 16 identified flaring events, all of which are shown in 45min periods in two panels of eight flares. One type of fast fluctuation that we have detected is generally associated with the rise or fall of bright flares, or at the peaks of bright flare emission, as seen for the flares 1A, 2A, and 5A. Similar minute time-scale variability has also been detected by Dodds-Eden et al. (2009). Another type of fluctuation is the point-to-point variability seen during some of the quiescent phases of low-level of activity, such as flares 1B, 1C, 2B, 3A, 4B, 6A, and 7A.

### 3.2. VLT NIR and Mid-IR Observations

The VLT observations used multiple bands to observe Sgr A\* on 2007 April 1–7, using the two instruments NACO (NIR) and VISIR (mid-IR). The results of these observations, which included the identification of seven flaring events are discussed in detail by Dodds-Eden et al. (2009). The brightest flare detected at  $3.80\mu\text{m}$  coincides with the brightest X-ray flare on April 4. Figure 5 shows a composite light curve of VLT observations with labeled flares using  $3.8\mu\text{m}$ ,  $2.12\mu\text{m}$  and  $1.66\mu\text{m}$  NIR bands. No NIR spectral index measurements are available for the detected flares. However, a  $3\sigma$  upper limit of 57 mJy is placed at  $11.88\mu\text{m}$  for the bright  $3.8\mu\text{m}$  flare on April 4 with a peak flux density of  $\sim 30$  mJy (see also Trap et al. 2009). The brightest NIR flare detected in this campaign consists of a cluster of overlapping flares that last for about two hours. The power spectrum analysis of NIR flares detected by the HST on 2007 April 4, as will be discussed in §5.3, shows a spectrum with a peak having a similar time scale. The second brightest flare detected by the VLT is identified as #6 in Figure 5. This flare precedes the bright NICMOS flare 5A (April 5), as shown in Figure 3e. These flares appear to be components of another period of flaring activity lasting for two hours.

### 3.3. X-ray Flaring Activity

The X-ray light curves between 2 and 10 keV with a time binning of 144s are shown in Figure 6. A total of five flares were observed: one in 2007 April 2 (labeled #1) with a peak X-ray luminosity  $L_{2-10\text{keV}} = 3.3 \times 10^{34} \text{ erg s}^{-1}$  and four on 2007 April 4 (labeled #2, #3, #4, #5) with peak  $L_{2-10\text{keV}} = 24.6, 6.1, 6.3, \text{ and } 8.9 \times 10^{34} \text{ erg s}^{-1}$ , respectively (Porquet et al. 2008). For the first time, within a time interval of roughly half a day, an enhanced incidence rate of X-ray flaring was observed, with a bright flare (#2, with a duration of 2900 s) followed by three flares of more moderate amplitude (#3, #4, #5, with durations of 300, 1300, and 800 s respectively). An enhanced rate of X-ray flares, although with lower amplitudes, was also reported in Bélanger et al. (2005) when one moderate and two weak flares were detected within a period of eight hours. These rates of X-ray activity (Porquet et al. 2008; Bélanger et al. 2005) are clearly higher than the typical duty cycle of one X-ray flare a day (Baganoff 2003). The brightest event on 2007 April 4 represents the second-brightest X-ray flare from Sgr A\* after the X-ray flare with  $\Gamma = 2.2 \pm 0.3$  on 2002, October 3, on record with a peak amplitude of about 100 times above the 2–10 keV quiescent luminosity<sup>20</sup> This bright X-ray flare exhibits similar light-curve shape (i.e., nearly symmetrical), duration ( $\sim 3$  ks) and spectral characteristics to the very bright flare observed on 2002, October 3 with XMM-Newton (Porquet et al. 2003). Its measured spectral parameters, assuming an absorbed power law model including the effects dust scattering, are  $N_{\text{H}} = 12.3_{-1.8}^{+2.1} \times 10^{22} \text{ cm}^{-2}$  and  $\Gamma = 2.3 \pm 0.3$  where the quoted errors are at the 90% confidence level. Therefore, the two brightest X-ray flares observed so far from Sgr A\* exhibited similar soft spectra  $\Gamma \sim 2.2 - 2.3$ . The spectral parameter fits of the sum of the three following moderate flares, while lower ( $N_{\text{H}} = 8.8_{-3.2}^{+4.4} \times 10^{22} \text{ cm}^{-2}$  and  $\Gamma = 1.7_{-0.6}^{+0.7}$ ), are compatible within the error bars with those of the bright flares. However, fixing the column density at the value found for the brightest flare (i.e.  $N_{\text{H}} = 12.3 \times 10^{22} \text{ cm}^{-2}$ ) leads to a larger photon index value for the sum of these moderate flares, i.e.  $\Gamma = 2.1 \pm 0.4$ .

---

<sup>20</sup>No detection was made using INTEGRAL in the 20–40 keV and 40–100 keV energy bands, leading to  $3\sigma$  upper limits of 2.63 and  $2.60 \times 10^{35} \text{ ergs s}^{-1}$ , respectively (Trap et al. 2009).

### 3.4. 43 GHz Time Variability: VLA

Figure 7a,b shows light curves measured during April 1–4 at 43 GHz with the VLA, using 87sec and 300 sec sampling, respectively. The light curve of the phase calibrator 17444-31165, which itself is cross calibrated by NRAO530, is flat and is shown at the bottom of each panel in Figure 7a. Since NRAO530 is not the primary calibrator, it provides a second check on instrumental stability and that its light curve was flat also.

The light curves of Sgr A\* show variations on a variety of time scales from as short as 30 min to longer than five hours at 43 GHz. The fluctuations on time scales of several hours  $\sim 5-6$  hours can be seen in Figure 7a,b. The slow flux variation over 5-6 hours could, in principle, result from the contamination of the emission by an asymmetric distribution of extended structures surrounding Sgr A\* especially when a compact configuration of the VLA is used. However, the contamination of flux by extended emission is minimal for  $uv$  data  $> 90k\lambda$  (or  $2.3''$ ) and the variability on several hour time scale is intrinsic to Sgr A\*. The contamination of extended emission was clearly seen at low elevations in the  $uv$  data  $< 90k\lambda$  at 43 GHz, and our 22GHz data taken simultaneously with 43 GHz data on 2007 April 1-4 were useless for time variability analysis because of the limited  $uv$  range (i.e.,  $< 70k\lambda$ ).

Most of the power of the 43 GHz fluctuations in four consecutive days of observations appears to fall in a range between 30 minutes and few hours, as best shown all light curves of Figure 7b. For example, fluctuations with  $\sim 1$ h time scale are detected at a level of 200 mJy in the April 1 and April 2 light curves centered near 13h and 11:15h UT, respectively. The light curve of April 4 shows largest flux variations at a level of  $\sim 40\%$  are seen to increase flux density from 1.1 Jy at 9h UT to 1.6 Jy near 15h UT. Another interesting feature of the April 4 light curve is the presence of multiple weak fluctuations at a level of 50 mJy on a time scale of  $\sim 20-30$  minutes. Figure 7c shows the light curves of April 4 for simultaneous observations at frequencies of 43.1851 GHz and 43.5351 GHz with a 30sec sampling time. The frequency separation between these light curves is 345 MHz. We note at least five 20–30 minute fluctuations that are seen in both light curves.

### 3.5. 14, 22 and 43 GHz Time Variability: VLBA

Figure 8a shows 43 GHz light curves based on VLBA observations on April 1, 5 and 11, with a 60 sec sampling time. Figure 8b shows the light curves at 22 GHz and 43 GHz on April 2 whereas Figure 8c shows the light curves at 15 GHz and 43 GHz on April 10. The flux density of Sgr A\* appears to vary on hourly time scale in all five days of observations as these light curves show the first measurements of the flux variation of Sgr A\* on a VLBA (milli-arcsecond) scale at several frequencies. Fluctuations in phase coherence and amplitude errors could produce significant changes in flux on short timescales. However, it is unlikely that calibration errors are similar at two frequencies, as shown in Figure 8.

One suspicious feature in all three lightcurves is a sharp rise after 12h UT in observations on April 1, 5 and 11. Similar sharp rise is also seen at 43 GHz on the light curve measured on April 2 in Figure 8b. The sharp rises occur just after the gap when calibration measurement made using a different observing setup are carried out on several days. Thus, these sharp rises repeat at the same sidereal time and thus are probably an unknown problem in the telescope or calibration procedures. However, it is most likely caused by slightly extended structure (i.e. the changing  $uv$  coverage).

### 3.5.1. 43 GHz Light Curve: VLBA and VLA Comparison

Because VLBA and VLA measurements on April 1 and 2 are taken simultaneously at 43 GHz, we compared the two light curves, as shown in Figure 9a,b with a 300 sec sampling time, respectively. The comparison of the light curves examines directly the localization of flaring events at radio wavelengths. The largest fluctuations in both VLA and VLBA light curves appear to agree with each other with the exception of sharp peaks noted in VLBA light curves. Peaks with hourly time scale durations occur in both light curves near 13h UT on April 1, as seen in Figure 9a. Similarly, the slow decreasing trend in the flux of Sgr A\* over few hours is seen in the light curves of 2007 April 2 at 43 GHz using both the VLA and VLBA, as shown in Figure 9b. The behavior of the light curves on hourly time scales measured with VLBA provides the first direct evidence that flaring activity arises from the innermost region of Sgr A\* on milliarcsecond (mas) scales. The size of the flare emission is dominated by interstellar scattering. The general agreement between the VLA and VLBA light curves imply that flaring region that has been detected is unresolved with the VLA.

Figure 9b shows also a sharp drop after a gap near 12:45h UT in the VLBA light curve which is suspicious and their cause should be investigated. We note additional drops in flux noted in the light curve of April 2 at 43 GHz near 10h, 11:30h and 14:30h, as shown at the bottom of Figure 9b. These drops in the 43 GHz flux do not precede by gaps in observations and are not seen in the VLA light curves at 43 GHz. As mentioned above, these drops are likely caused by the slightly extended structure of Sgr A\*.

There are also discrepancies between the two light curves. One is the different values of “average levels” of flux taken in the light curves measured with the VLA and VLBA. In all the measurements shown in Figures 7a and 8a,b the average-level of VLBA flux appears to be lower than that of the VLA by  $\sim 200$  mJy. The uncertainty in the absolute flux density calibration of Sgr A\* at 43 GHz using VLBA and VLA could easily explain this discrepancy. The second possibility is the emission from Sgr A\* could be contaminated by extended emission from the surrounding medium, as measured with the VLA, even though we have selected data with  $uv > 100k\lambda$ . Lastly, it is possible that this discrepancy could be explained by a core-halo structure of emission from Sgr A\* in which the halo component is resolved out in VLBA observations. Future simultaneous VLA observations using its most extended array configuration and VLBA should be able to examine closely the reason for this discrepancy.

Another curious feature of the VLBA light curve is the possible presence of fast fluctuations detected on short time scales, as seen in Figure 9c. One of these fluctuations is seen in the decaying segment of the strong flare near 14.3h on 2007 April 1 UT. Fast fluctuations are also noted in the VLBA light curve on April 2, as shown in Figure 9b, though there are differences between VLA and VLBA light curves that do not match each other and thus need to be confirmed in future observations. Fluctuations on time scales of  $<10$  min do not correlate well between the VLA and VLBA data and probably indicate that the error bars are somewhat underestimated.

The top and bottom panels of Figure 9d show blow-up view of the time interval between 13.3h and 14.5h UT based on VLA and VLBA observations, respectively. In spite of the poor sampling of the VLA data, both light curves show similar behavior but there are also discrepancies. We note the change in the flux of Sgr A\* in the decaying part of the light curve using VLA and VLBA data is roughly 0.3 Jy.

### 3.6. CSO 350 $\mu$ m, 450 $\mu$ m, 850 $\mu$ m Light Curves

Figure 10 shows the light curves at three submillimeter wavelengths. The data have been smoothed to increase the signal-to-noise ratio with a sampling time of  $\sim 6.5$  minutes. As at radio wavelengths, the flux of Sgr A\* appears to be varying on hourly time scales. The largest Sgr A\* increase is detected at the beginning of the observation near 13:30 UT on 2007 April 1. The highest 450 $\mu$ m flux variation is seen at the beginning of the observation on 2007 April 3. These light curves show evidence for hourly and intraday variability at 450 $\mu$ m, at a level of 14%. The mean daily flux of Sgr A\* at 450 $\mu$ m is  $\sim 3 \pm 0.25$  Jy.

Figure 10b shows some of the first variability of Sgr A\* at 350 $\mu$ m. The flux increase on 2007, April 4 over 5 hours is about 50% of the initial flux of Sgr A\*. This steady increase of flux density over several hours is seen to continue at 90 GHz (see section 3.10). Figure 10c shows the light curve at 850 $\mu$ m on 2007, April 6. Unlike the other submillimeter light curves shown here, this light curve appears to show time variability on a time scale of  $\sim 10$  minutes as seen near 13h:20m UT. Such sharp variations at 850 $\mu$ m at such a short time scale resembles the recent light curve obtained with a different instrument (LABOCA of APEX) (Eckart et al. 2008). The reality of such a short time scale variation needs to be confirmed.

### 3.7. SMA: 230 GHz Light Curves

Figure 11 shows the light curves taken from four days of observations with the SMA at 230 GHz. The 2007 April 1 data shows an asymmetric profile indicating a duration of possibly  $\sim 4$  hours considering that there is a gap between 16h and 17h:30m UT. Similar submillimeter characteristics have been seen recently at 850 $\mu$ m (Yusef-Zadeh et al. 2008). The 2007 April 3 light curve shows an emission peak near 14h UT, before a slow decay that lasts for about 4 hours. The light curve obtained with SMT on the same day and at the same wavelength showed the rising part of the light curve suggesting that the duration of the flare on this day could be as long as 8 hours. The 2007 April 4 light curve shows a typical profile of submillimeter flare emission, except for a dip in the flux at a level of 100 mJy near 14h UT. The April 5 data shows a light curve with multiple peaks as the light curve decays. The typical time scale for this variation is between  $\sim 1$ -2 hours. The overall percentage of flux variation during 6 hours of observations is between 10% and 30%.

### 3.8. SMT 250 GHz Light Curves

The SMT light curves of Sgr A\* and calibrators (in blue) for 2007, April 1-4 are shown in Figure 12. Because SMT and SMA observed Sgr A\* at the same wavelength considering the broad bandwidth of the SMT, we compared the SMT light curves with those of SMA on April 1, 3 and 4. An increase in flux of  $\sim 1$  Jy in the rising part of the light curve is seen between 10h UT and 14h UT on 2007, April 3. This increase is similar to the decrease in the flux of Sgr A\* found in the decaying part of the SMA light curve, as seen in Figure 11.

The low spatial resolution of the SMT results in a higher background level for the Sgr A\* light curve. The discrepancy in the zero level flux of Sgr A\* using SMT and SMA on April 3 and 4 is due to the fact that the emission from Sgr A\* using SMT is contaminated by  $3.5 \pm 0.2$  Jy of flux from extended features. If this flux is subtracted from the April 3 data and combined with the SMA light curve, the duration of the variability is estimated to be  $\sim 6$  hours.



The 2007 April 4 data show that the flux of Sgr A\* did not change substantially. We note similar behavior in the SMA light curve, as shown in Figure 11. We also note a curious dip in the flux of Sgr A\* near 14:10h UT and 13:50h UT lasting for about 15 minutes in the SMT and SMA light curves, respectively. These similarities between light curves obtained with a single channel single-dish telescope and an interferometer give us confidence in the reality of the observed features.

The 2007, April 1 shows the most dramatic flux variation of  $\sim 2$  Jy. The reality of this feature can not be confirmed as different calibrators were used at the beginning of the observation. However, a  $3.6 \pm 0.2$  Jy subtraction from the SMT data matches well with the SMA data, thus suggests that the sudden rise 11h UT is likely to be real.

### 3.9. IRAM 230 GHz Light Curves

Figure 13 shows the light curves of the two days of IRAM observations on 2007 April 3 and 4. There is no evidence for any flux variations in these observations. The April 4 light curve overlaps with the biggest NIR/X-ray flare detected during this campaign. However, there is no indication that the 230 GHz flux density changed by more than  $1.5 \pm 0.5$  Jy between 5h and 7h UT, during which the bright NIR/X-ray flare took place.

### 3.10. NMA 140 GHz and 230 GHz Light Curves

Figure 14 shows the NMA light curves of Sgr A\* and 1744-312 based on two days of observations under excellent weather conditions. The flux of the calibrator remains flat during these observations, whereas the flux of Sgr A\* increases by  $\sim 0.5$  Jy at 90 GHz on April 3. The April 4 light curve shows a slight increase at 146 GHz before decaying strongly by more than 1 Jy. The duration of the flare is roughly 2 hours.

### 3.11. CARMA Light Curves

Fig 15 shows the light curves of Sgr A\* and the calibrator 1733-130 at 94 GHz taken for four days of observations on 2007, April 2-5. There is flux variation on short and long time scales in all days of observations. There is concern on the variation of the calibrator evident in almost all days of observations. Due to this uncertainty, we compared the light curves with other 94 GHz and 43 GHz measurements and we believe the large scale variation may reflect the intrinsic variable emission from Sgr A\*. However, the flux variation of Sgr A\* on short time scale may not be valid.

### 3.12. GMRT Light Curves

Figure 16 shows the light curve measured with GMRT at 1.28 GHz. As we observe Sgr A\* at long wavelengths, the light curve of Sgr A\* may be contaminated by the extended nonthermal emission surrounding Sgr A\* as well as by interstellar scattering which becomes more important at long wavelengths. In order to avoid the contamination by extended emission, we used the  $uv$  data at the highest elevation as well as restricted the  $uv$  distribution be greater than  $80k\lambda$ . Also, interstellar scintillation is expected to operate on longer time scales than hourly time scales that we are sensitive to. Thus, a flux variation of  $\sim 80$  mJy over four hours reflects the variation of flux

of Sgr A\* at 1.28 GHz.

## 4. Analysis

### 4.1. NIR Flare Statistics

Given the ability of HST to produce continuous observations over many 45 min orbital visibility periods, along with its long-term photometric stability, the NIR NICMOS data provide an excellent way to investigate the flare strength distribution over many flare episodes. Figure 17a shows a histogram of the NICMOS  $1.70\mu\text{m}$  net flare emission for the 7 days of data obtained in this campaign. The net flare emission is measured by first subtracting the background emission for each day before the excess flux above the background is selected. Thus, the selected data points do not sample the peak flare emission but rather the flux associated with flaring activity. The peak of values centered at a net flux of zero represents the emission from Sgr A\* during “quiescent” periods. The positive half of the histogram, on the other hand, shows a tail of flare emission events extending out to  $\sim 10$  mJy. The “quiescent” distribution is best fitted with a Gaussian, which is expected from the level of random noise in the observations. The tail of flare emission can be fitted with a power-law distribution having an index of  $-1.19 \pm 0.27$  and a low-energy cutoff at  $S_\nu = 1$  mJy. The dotted line in the figure shows the result of simultaneous Gaussian and power-law fits to these two components.

Yusef-Zadeh et al. (2006a) reported that distribution of flare activity seen in our more limited 2004 NICMOS observations could be fitted by two simultaneous Gaussians profiles. A reanalysis of those data, however, now show that a power-law distribution with a low-energy cutoff yields a good fit to the 2004 epoch data as well. Figure 17b shows a histogram of the 2004  $1.60\mu\text{m}$  data, with Gaussian and power-law fits to the two components shown by the broken lines. The best power-law fit to these data has an index of  $-1.11 \pm 0.13$ , with a low-energy cutoff of  $S_\nu = 0.25$  mJy. This is remarkably consistent with the best-fit power-law index of the 2007 data. We note that the fraction of observing time that flare activity has been detected in the 2004 and 2007 campaigns is  $\geq 32\%$  and  $\geq 37\%$ , respectively.

The NIR flare histograms for the two epochs show that the probability of measuring flux  $S_\nu$  at any instant is approximately proportional to  $1/S_\nu$ . Presumably this reflects the statistics of the flaring behavior of Sgr A\* at NIR wavelengths. To explore this we construct a simple phenomenological model for the flaring by simulating a light curve and then sample it to construct a simulated histogram. This model shows that the observed  $1/S_\nu$  behavior arises quite naturally, but does constrain the statistics of the flaring.

Our phenomenological model represents the flaring as a sequence of 100 Gaussian profiles occurring over 100 arbitrary time units, with flare  $i$  characterized by peak flux  $S_i$ , timing of the peak  $t_i$ , and standard deviation of the flare  $\sigma_i$ , so that the net light curve may be written as

$$S_\nu(t) = \sum_{i=1}^{100} S_i \exp\left(-\frac{(t - t_i)^2}{2\sigma_i^2}\right). \quad (1)$$

The parameters  $S_i$ ,  $t_i$ , and  $\sigma_i$  are drawn randomly and uniformly from the ranges  $[0, 1]$ ,  $[0, 100]$  and  $[0, \sigma_{\text{max}}]$ , respectively, and the resulting light curve is evenly sampled every 0.2 time units to create a flare histogram. Note that  $\sigma_{\text{max}}$  is the only independent parameter of this model, as increasing the number of flares and changing the maximum flare amplitude can be accommodated by rescaling

the flux and time units. In addition, changing the sampling rate or the number of flares does not affect the statistics, provided that the light curve has already been adequately sampled (which is the case for our adopted sampling rate of 50 per time unit). We find that  $\sigma_{\max} \lesssim 0.5$  yields the observed  $1/S_\nu$  behavior.

A typical simulated light curve and the corresponding histogram for  $\sigma_{\max} = 0.5$  are given in Figures 18a and b, respectively. The slope of  $S_\nu^{-1}$  is drawn on Figure 18b. Larger values of  $\sigma_{\max}$  lead to significant overlap between flares, tending to give a flatter dependence of the flux probability on  $S_\nu$ . This does not, of course, prove definitively that the flares behave as given by equation 1. Other choices of functional form or different statistics for  $S_i$  may also yield the  $1/S_\nu$  behavior of the histogram. It does, however, seem to require that the flare events do not significantly overlap each other.

#### 4.2. Spectral Index Distribution Between $1.45\mu\text{m}$ and $1.70\mu\text{m}$

We have constructed a log-log distribution of spectral index based on the NICMOS  $1.45\mu\text{m}$  and  $1.70\mu\text{m}$  data. Figure 19 shows the "color" distribution of all the data selected with signal-to-noise  $S/N=3$ . The diagonal line (in red) shows the spectral index of  $\beta=0.6$ , where  $F_\nu \propto \nu^{-\beta}$ . For comparison,  $\beta$  of -4, -2, 2, and 4 are also plotted. This figure shows a tendency for the spectral index of low flux values to be steeper than 1, whereas the high flux values are represented by a flatter distribution of spectral index. Because the data points used in making Figure 19 are not taken simultaneously at the two different wavelengths, we attempted to estimate spectral index values of adjacent data points, where the flux of Sgr A\* is not varying rapidly, such as during the fast rise or fall of individual flares.

We identified five sets of data points associated with five different flares during which the overall Sgr A\* flux is not varying rapidly. Table 1 shows the corresponding flux and spectral index values using data sampled at 144 sec intervals. The two brightest flares, 5A and 2A, have spectral indexes  $0.73 \pm 0.16$  and  $0.97 \pm 0.27$ , whereas the weaker flares have indexes steeper than  $\beta=1.5$ . These individual measurements are consistent with the spectral index trend shown in Figure 19. We also find that the spectral index of the brightest flares are consistent with recent Keck measurements, which yield a spectral index of 0.6 (Hornstein et al. 2007). The spectral index of low flux values is also consistent with VLT measurements, which show a steep spectrum for weak flares (Eisenhauer et al. 2005; Gillessen et al. 2006). These measurements suggest that the spectral index of flares varies with the NIR flare strength, support earlier measurements by Gillessen et al. (2006) and disagree with measurements by Hornstein et al. (2007) who claim a constant spectral index in NIR wavelengths. The variation of spectral index with flare emission at NIR wavelengths has important implications on the inverse Compton scattering mechanism of X-ray and soft  $\gamma$ -ray emission from Sgr A\* (Yusef-Zadeh et al. 2006a). It is possible that weak flares with a steep energy index of particles are associated with low-level activity of the accretion disk of Sgr A\*, whereas the bright flares represent the hot magnetically-dominated events that are launched from the disk. Polarization characteristics of the weak and strong flares may constrain models of the flare emission.

### 4.3. NIR Power Spectrum Analysis

Genzel et al. (2003) had reported a possible 17 min NIR periodicity with implications for the spin of the black hole. Our previous 2004 HST data (Yusef-Zadeh et al. 2006a) showed a marginal detection of power at  $33 \pm 2$  minutes. We investigated the power spectrum of flare data taken with the new NICMOS measurements. Lomb-Scargle simulations are used to search for periodicities in the spectra of our unevenly-spaced NIR flares (Scargle 1982). The only artificial signals that are considered to be significant are the  $\sim 90$  minute orbital period of the HST and the 144 sec filter switching cycle. Thus, any signals at these frequencies and their harmonics are most likely not attributable to Sgr A\*. Within the seven periods of HST observations, the only one that shows significant power is on 2007, April 4. The time scale for the variability is  $\sim 2$  hour. Figure 20 shows the power spectrum as a solid line and the dotted lines show the the spectrum of the noise using power-law distributions. The only signals above the 99% light curve of the simulated power spectrum have time scales of two hours. In order to determine the significance of power at a given frequency, we employed a Monte Carlo technique to simulate the power-law noise following an algorithm that has been applied to different data sets (Timmer & König 1995; Mauerhan et al. 2005). 5000 artificial light curves were constructed for each time segment. Each simulated light curve contained red noise, following  $P(f) \propto f^{-1.5}$ , and was forced to have the same variance and sampling as the original data.

Given the approximately  $\sim 6.5$  hours of HST data taken on 2007, April 4, there was evidence of enhanced variability on timescales of  $\sim 2$  hours. The lack of any significant power between 17 and 20 minutes supports the results from an earlier analysis of HST data in 2004 (Yusef-Zadeh et al. 2006a). Recent analysis of data taken with the combined VLT and the Keck observations shows no significant power on short time scales (Do et al. 2008; Meyer et al. 2008).

### 4.4. X-ray vs. NIR flare Emission Mechanism

As described in section 3.3, there are a total of five X-ray flares detected in the present observing campaign. The strongest X-ray flare (#2) coincided with a strong NIR flare. HST observations detected three of the remaining four X-ray flares (#1, #4 and #5) corresponding to flares 2A, 4A and 4B, respectively. Figure 21a,b show the X-ray light curves of these newly detected NIR flares at  $1.70 \mu\text{m}$ . Table 1 presents the flux and spectral index of the NIR flare 4A. We discuss below a model to explain the production of X-ray flares and their physical relationship to NIR flares and the quiescent submillimeter emission from Sgr A\*.

There are two ways that synchrotron flaring in the infrared can produce an X-ray flare by inverse Compton scattering. First, submillimeter seed photons may be upscattered by the transient population of relativistic electrons whose synchrotron emission is producing the infrared flare. Second, a proportion of the NIR photons emitted during the flare will be upscattered by the population of relativistic electrons that is responsible for the quiescent submillimeter emission. Figure 22a shows a schematic diagram of the second scenario to produce X-ray emission. These two scenarios were considered to be degenerate in producing the needed X-ray flux (Yusef-Zadeh et al 2006). Below, we argue that this degeneracy is removed by the optical depth effects of the quiescent emission and that the second ICS possibility is more consistent with observations.

Dodds-Eden et al. (2009) have recently shown that matching the observed X-ray and NIR fluxes for flare #2 in the first ICS scenario – in which submillimeter photons are upscattered – requires an

uncomfortably small submillimeter source size ( $R_Q \lesssim R_s$ ). In addition, although the other flares (e.g., Yusef-Zadeh et al. 2006) can be modeled with source sizes of a few Schwarzschild radii and field strengths in the 10 G range, the electron pressure of the GeV electrons in the NIR-emitting region exceeds the magnetic pressure by more than an order of magnitude, and their acceleration and confinement becomes problematic (this is also the case for flare #2). Thus, we now turn to the second mechanism to produce X-ray emission by ICS.

The second scenario – upscattering of NIR photons by the quiescent population of electrons – contributes the same X-ray intensity as the first if both the submillimeter and NIR emission regions are optically thin. Dodds-Eden et al. (2009) argue that actually this contribution is necessarily smaller, but only by artificially restricting the upscattering of NIR photons to occur within the NIR source region. NIR photons will escape into the submillimeter source region and be upscattered there as well, and the overall emission will indeed be of similar magnitude to that produced by submillimeter seed photons.

In fact, the contribution of the second scenario is significantly greater than the first because the submillimeter source region is optically thick below 1000 GHz, and therefore the observed quiescent submillimeter flux is produced by a fraction of the underlying electron population. This emission region is optically thin to NIR photons, and so all of these electrons are available to upscatter NIR seed photons to X-ray energies. As a result, the ICS luminosity produced through this second scenario will dominate that produced by the first.

To estimate the resulting ICS flux we characterize the electron population responsible for the quiescent submillimeter emission by electron number density  $n_e$ , a relativistic Maxwellian energy distribution at temperature  $T$ , and a quasi-spherical region of size  $R$ . These electrons upscatter the NIR seed photons arising from synchrotron emission from the relativistic electrons producing the NIR flare with observed flux  $S_\nu$  at the earth. The ICS flux depends on the direction-averaged intensity,  $J_\nu$ , of seed photons which in turn depends on the location and size of the flare emission region; we estimate this to order of magnitude by simply assuming that the flare region is of similar size to the submillimeter emitting region, such that

$$J_\nu = \frac{d^2}{\pi r^2} S_\nu, \quad (2)$$

where  $d = 8$  kpc is the distance to the Galactic Center.

The energy of the upscattered photons is small compared to the MeV-range of the electron energies, so we can use the Thomson cross-section. To a good approximation, inverse Compton scattering by an electron with energy  $E \gg m_e c^2$  boosts photon energies by a factor  $(E/m_e c^2)^2$  irrespective of the scattering angle. The differential ICS luminosity per unit energy interval is then simply

$$L(E_\gamma) = \frac{4\pi\sigma_T}{h} \int N(E) J_\nu dE \quad (3)$$

where  $N(E) dE$  is the *total* number of electrons in the energy interval  $[E, E + dE]$ , and  $J_\nu$  is the direction-averaged intensity of the seed photons at frequency  $\nu = \frac{3}{4} E_\gamma / (E/m_e c^2)^2$ . For temperatures in excess of a few MeV, the vast majority of the electrons have  $v \approx c$  and the relativistic Maxwellian distribution can be approximated by

$$f(E) \approx \frac{1}{2kT} \left( \frac{E}{kT} \right)^2 \exp \left( -\frac{E}{kT} \right) \quad (4)$$

and then  $N(E) = \frac{4}{3} \pi R^3 n_e f(E)$ .

If the spectrum of the seed photons is a simple power-law, ie.  $S_\nu = S_0(\nu/\nu_0)^{-\beta}$ , or a broken power-law, then the resultant ICS spectrum may or may not have the same spectral index in NIR and X-ray wavelength bands, respectively. In the case of the strongest X-ray flare (#2) which coincides with a strong NIR flare, the NIR spectral index and X-ray spectral index are different with  $\beta_{X-ray} = 1.3 \pm 0.3$  (90% confidence) whereas  $\beta_{NIR} < 1.0$  ( $3\sigma$ ) (Dodds-Eden et al. 2009). In the context of the second ICS scenario, this could be explained by a broken power law of NIR emitting electrons with a steeper spectral index shortward of  $3.8\mu\text{m}$ , perhaps resulting from a shorter time scale for synchrotron cooling of electrons at high energies. For a simple power law, the differential luminosity is

$$L_\gamma(E_\gamma) = \frac{8\pi\sigma_T d^2}{3h} \Gamma(3 + 2\beta) S_0 n_e R \left( \frac{E_\gamma}{E_{\gamma 0}} \right)^{-\beta} \quad (5)$$

where  $E_{\gamma 0} = 4/3(kT/m_e c^2)2h\nu_0$ .

By way of illustration we adopt reasonable choices for  $R$  and  $n_e$ , i.e.  $R = 10 R_s$ ,  $n_e = 10^7 \text{ cm}^{-3}$ , and compute the ratio of 2–10 keV luminosity to  $2.2\mu\text{m}$  flux as a function of spectral index  $\beta$ . The results for electron temperatures of 3, 5, 7, and 10 MeV are plotted as solid curves in Figure 22b. The X-ray to NIR flux ratio declines with increasing spectral index  $\beta$  because X-rays in the 2–10 keV band are produced by upscattering of photons that are shortward of  $2.2\mu\text{m}$ , and for fixed flux at  $2.2\mu\text{m}$  there are less of these as  $\beta$  is increased. Also shown for comparison are the measured ratios and spectral indices of the 7 coincident IR and X-ray flares seen to date, (Yusef-Zadeh et al. 2006; Belanger et al. 2005; Eckart et al. 2006; Hornstein et al. 2007; Marrone et al. 2008; Porquet et al. 2008; Dodds-Eden et al. 2008; this paper). We conclude that the fluxes of the observed X-ray flares are broadly consistent with this ICS model.

In this scenario, the flux in the 2–10 keV band is produced predominantly by upscattering of photons with wavelengths shortward of  $1\mu\text{m}$ . This may explain why the width of the bright 2007 April 04 flare is less in X-rays than in the infrared: the infrared flare may have decayed more rapidly shortward of  $1\mu\text{m}$  than at  $3.8\mu\text{m}$  and so the X-ray flux declines without a corresponding decrease at NIR wavelengths.

The extent of the submillimeter-emitting electron population may on occasion give rise to significant time delay between infrared flaring and their X-ray counterparts. A sufficiently hard IR flare would lead to X-ray production by inverse Compton scattering on the extended  $\sim 1000 R_s$  outer envelope of low-temperature electrons, producing weak post-main-flare X-ray emission lasting for tens of minutes after the main flare has subsided. Theoretically, the electron temperature is set by a balance between heating by Coulomb interactions with protons and by plasma effects and synchrotron cooling.  $kT$  for the protons is a reasonable fraction of their virial energy because of inefficient cooling in the accretion flow. This implies that the protons should be non-relativistic at  $\sim 1000 R_s$ , with MeV-range energies. The electrons are likely to have similar energies because of formalization and are then mildly relativistic. Empirically, Loeb & Waxman (2007) estimate from the radio/submillimeter spectrum that the electron temperature is a few MeV all the way out to  $1000 R_s$ . Detection of these “echoes” would confirm the scenario proposed here and help determine the size of the outer region which is rendered inaccessible to direct by the effects of interstellar scattering in radio wavelengths.

#### 4.5. NIR vs. Radio flare Emission

The relationship between radio and NIR flare emission has remained unexplored due the very limited simultaneous time coverage between radio and infrared telescopes such as the VLA and the VLT or the Keck. The continued variations of the radio flux on hourly time scale also makes the identification of radio counterparts to infrared flares difficult. In spite of this, the strong flaring in NIR/X-ray wavelengths on 2007, April 4 has given us an opportunity to examine whether there is a correlation with variability at radio frequencies. One of the key motivation of our observing campaign was to examine the adiabatic expansion picture of flaring activity of Sgr A\*. One of the prediction of this model is a time delay between the peaks of optically thin NIR emission and optically thick radio emission. This implies a NIR flare with its short duration is expected to have a radio counterpart shifted in time with a longer duration. Below, we argue for a radio counterpart to a strong NIR flare by shifting and stretching the time axis of the NIR light curve.

Figure 23a shows composite light curves of Sgr A\* obtained with VLA, VLT, HST and XMM on 2007, April 4. These light curves show three peaks in each of the radio and NIR light curves. The flux increase at 43 GHz is  $\sim 40\%$  which is higher than those from the first three days of VLA observations which is  $\sim 20\%$ . We also know that there was no significant variation at 240 GHz during the period in which the strong NIR/X-ray flare took place. The IRAM-30m observation shows an average flux of  $3.42 \pm 0.26$  Jy between 5 and 6h UT when the powerful NIR flare took place. The flux is mainly arising from the quiescent component of Sgr A\*. Comparing the light curves of the the 43 and 230 GHz data, there is no evidence for a simultaneous radio counterpart to the NIR/X-ray flare with no time delays.

We now argue that the radio flare detected between 10h and 15h UT is a time-delayed counterpart to the NIR/X-ray flare for the following reasons: i) the highest percentage of the flux increase at 43 GHz on 2007, April 4 compared to other three days of radio observations, ii) the presence of three peaks in NIR and radio light curves and iii) the lack of significant flux variation above the quiescent flux of Sgr A\* at 240 GHz during the NIR/X-ray flaring events. We suggest that flare emission at 43 GHz is time delayed with respect the NIR/X-ray flare emission. To explore this further, we have empirically shifted and stretched the time axis of the NIR/X-ray light curves by 3.05 hours and a factor of 5.7, respectively. Figure 23b presents the shifted and stretched NIR/X-ray light curves in the top two plots. The bottom plot shows a baseline subtracted radio light curve. The subtraction is used to remove the contribution by the quiescent flux. The shift and stretch operation to the time axis is carried out by eye and then examined by cross correlating the NIR and time-delayed and time-stretched 43 GHz light curves. We find that the best best fit shows a peak in the cross correlation plot of  $3.49^{+2.4}_{-14.9}$  min which is consistent with zero. The  $1-\sigma$  error to the cross correlation peak of the shift is given in Table 2.

Given that NIR/X-ray and radio emission are expected to be optically thin and thick, respectively, the similarity in the substructures in radio and NIR light curves and the way that they trace each other, as shown in Figure 23b, are remarkable. For example, two peaks before and after 12h UT and one near 14h UT are detected in both NIR and radio light curves. The dips near 13:30h UT and 13h UT are also seen, though the shape of the radio appears to shifted with respect to the NIR dip. To make a stronger case that the NIR and radio flares are related to each other, the morphological agreements between radio and NIR could have been improved, had we used a a varying time shift to the NIR data between the first and second halves of the observation. A detailed account of these light curves in the context of adiabatic cooling plasma model will be given elsewhere.

Given that there is continuous coverage for about ten hours between 5h-15h UT in X-ray, NIR and radio wavelengths using XMM, VLT, HST, IRAM and VLA with an exception of a two-hour gap between 7 and 9h UT in radio wavelengths and a 2.5-hour gap between 10.5h and 13h UT in NIR wavelengths, we believe the lack of association between flaring activity in NIR and radio wavelengths is highly contrived. Obviously, we can not prove conclusively that radio flare seen on April 4, 2007 is associated with the NIR/X-ray flare because of two gaps in our coverage. Nevertheless, the comparison of the 43 GHz light curve with the NIR data suggest that these variations are tied closely with each other.

#### 4.6. Cross-Correlation of Light Curves

As pointed out in the previous section the adiabatic expansion picture of the flare emission from Sgr A\* makes the predictions that i) the NIR and X-ray emission are expected to be simultaneous and therefore optically thin whereas optical depth effects become important at lower frequencies, thus a time delay is expected between their peak emission. To examine these issues, a great deal of data have been obtained simultaneously in this campaign, which allows us to cross-correlate the multi-wavelength data for each day of observation. The light curves that we have presented thus far indicate that the flux of Sgr A\* is constantly changing as there is low-level flare activity in almost all wavelength bands. There are very few measurements that were taken simultaneously with the same time coverage with few exceptions. Altogether there are four detected NIR flares that have shown X-ray counterparts. There is no evidence that there is time delay between the peaks of any of the detected flares, thus supporting the fact that both NIR and X-ray emission are optically thin. The lack of time delay places a strong constraint on the ICS picture.

The strong flare observed on 2007 April 4 is one example in which a cross correlation peak with small error bars can be obtained. The cross-correlation of the light curves at X-ray and NIR wavelengths is shown in Figure 24a. The peak of the cross-correlation shows that X-ray emission is delayed by 29 seconds with a one-sigma error bar of -6.5 and +7.0 minutes. In the ICS picture, as described in section 4.4, the region from which NIR photons are upscattered should be less than 0.8 AU. Dodds-Eden et al. (2009) presented first the simultaneity of X-ray and L/bands to within one sigma error bar of three minutes.

There were no simultaneous observations that were taken with the same instrument except with the VLA and NMA but with a small frequency separation. In spite of the small separation between the observed frequencies at 134 GHz (2.23 mm) and 146 GHz (2.05 mm), the data are taken simultaneously on 2007, April 4 with the NMA. The cross correlation of the light curves at these frequencies, as shown in Figure 24b, peaks with  $6^{+6.6}_{-4.8}$  minutes time delay.

Due to the limited UT coverage with individual telescopes as well as the lack of strong flaring event in this campaign (with the exception of the strong NIR/X-ray flare on 2007, April 4), the cross correlation of the light curves had difficulty following accurately the time evolution of a flare as a function of frequency. In spite of these difficulties, we have obtained cross-correlation plots of low-level fluctuations evident in four light curves. Although most of the individual cross correlation peaks have low signal-to-noise, the peaks of optically thick emission all show a tendency to lag rather lead, thus, consistent with the adiabatic expansion picture of flare emission. We have selected the best light curves to show the time lag but in fact almost all light curves systematically showed a time lag rather than a lead in their cross correlation peaks, though low signal to noise ratios. We believe the data presented here supports the plausibility of the time delay, as has also been shown



in earlier cross-correlation measurements. We give four examples that indicate higher probability that the peak flare emission at high frequencies leads those at low frequencies.

Figure 25a presents the cross-correlation plot of the light curves taken at  $450\mu\text{m}$  using the CSO and 230 GHz using the combined data taken from the SMA and SMT on 2007 April 3. The cross-correlation plot at the bottom of the panel shows a maximum likelihood time delay at  $1.32^{+1.66}_{-0.69}$  hours. Another example shows the evidence for a time delay between 1.2mm (230 GHz) and  $450\mu\text{m}$  wavelength bands on 2007, April 1 and the cross correlation plot is displayed in Figure 23b. The cross-correlation peak between these wavelength bands is  $0.24^{+1.48}_{-0.04}$  hours time delay.

The cross-correlation peak between  $1.70\mu\text{m}$  and 1.3mm wavelengths on 2007, April 5 is shown in Figure 23c and gives a time delay 2.64 hours with a  $2\sigma$  uncertainty range of -1.66 to 3.3 hours. The NIR data for this plot combined the  $1.70\mu\text{m}$  data of HST (flare 5A of Fig. 3) and the  $3.8\mu\text{m}$  VLT data (flare 6 in Dodds-Eden et al. 2009). Because the spectral index of the HST data is determined, we assumed that the preceding flare detected by the VLT at  $3.8\mu\text{m}$  has the same spectral index and its duration is continuous with the brightest HST flare emission seen in this campaign.

As discussed before, the strongest NIR/X-ray flare was detected on 2007, April 4 showing a peak at 5.9h UT with a full duration of about two hours in NIR wavelengths. The 2.1mm (140 GHz) light curve taken with IRAM during this period of flaring activity placed a constraint by showing a lack of flux variation with a one-sigma error of 0.26 Jy at millimetre wavelength during a strong flaring activity.

## 5. Discussion

### 5.1. Adiabatic Expansion of Hot Plasma

Our campaign did not uncover clear time delay signatures due to lack of overlapping coverage, poor signal to noise and atmospheric variations in the submillimeter and a lack of dramatic submillimeter flaring events during the campaign. The data presented here show an increasing chance of high frequency flare emission leading the low frequency emission when simultaneous data between 43 GHz, 94 GHz, 230GHz, 0.45mm and  $1.70\mu\text{m}$  are examined. It is only the collection of the cross correlation plots that make the time delay between the peaks of flare emission compelling. One likely example is seen in the light curves at CARMA and the VLA on 2007 April 02 at frequencies of 94 GHz and 43 GHz respectively (see Fig. 25d).

Another example that could be considered is the light curve at 43 GHz using the VLA which began covering the flare 4.5 hours after the start of the NIR flare on 2007 April 4. The morphology of the peaks in the two light curves appears to show a rise of flux followed by flattening of the emission. Figure 23b shows the comparison of the two light curves by shifting the NIR light curve by about three hours and stretching by a factor of 5.7. We suggested that shifting and stretching of the light curves serve as the time delay and duration of flare as it evolves in time. The shift of this magnitude falls within the uncertainty of the time delay noted between the millimeter and NIR peak flare emission (see Table 2). The stretching of the NIR light curve by a factor of 5.7 can be also viewed in the context of the expanding blob model of an initial flare or a compact blob observed in NIR followed by the expansion of a blob of hot plasma emitting in radio wavelengths. Individual NIR and radio flares show typical durations of  $\sim 20$  min and 2 hours, respectively. The ratio of the observed durations is similar to the stretching factor that was applied to the time axis

of the NIR light curve of flare emission.

## 5.2. Power Law vs. Relativistic Maxwellian Distributions of Flares

Previously we have modeled the time delays at submillimeter to radio frequencies in the expanding hot plasma model assuming that the accelerated particles have a power-law energy distribution. This is motivated by the long time scale of the flares compared to the synchrotron loss time for the expected magnetic field strengths of 10–30 G. These models assume a homogeneous sphere threaded by a uniform magnetic field. As the region expands, the relativistic particles cool by adiabatic expansion with  $E \propto 1/R$  and the magnetic field is diluted as  $B \propto R^{-2}$  because of flux freezing. Assuming that the relativistic electron energies run between 1 MeV and 100 MeV and that they are in equipartition with the magnetic field, the models are characterized by the particle spectral index,  $p$  (with  $n(E) \propto E^{-p}$ ), the expansion speed  $v$  (assumed constant), and the timing and amplitude of the flaring at a single frequency. From this we can infer a magnetic field strength  $B$  and the size of the emitting region at  $t_0$ ,  $R_0$ . Figure 26a shows an approximate fit to the CARMA and VLA data obtained on 2007 April 02 using two flares. The derived parameters of the first flare at 10.9 h UT are  $p = 0.5$ ,  $R_0 = 3.6 R_s$ ,  $v = 0.070c$ , and  $B = 15 G$ , while the later flare at 14.7 hr UT has  $p = 1.5$ ,  $R_0 = 9.8 R_s$ ,  $v = 0.065c$ , and  $B = 13 G$ . These numbers should be regarded as illustrative given the rough fitting, the simplicity of the model, and the freedom in choosing the baselines at each frequency.

While a power-law electron spectrum is plausible, the inferred spectra are significantly harder than the  $E^{-2}$  expected on the basis of the simplest version of diffusive shock acceleration. This suggests that the derived power law may instead be the effective power-law of the particle energy spectrum over the small (5%) range of initial energies relevant to our observing frequencies at 96 GHz to 43 GHz. Other spectral forms are easily introduced within the context of this model. By way of example, in Fig. 26b we show the “best” relativistic Maxwellian model, with the particle spectrum characterized by the electron temperature  $T_e$  at time  $t_0$  instead of  $p$ . The parameters in this case ( $kT_e = 0.25$  keV,  $R_0 = 4.4 R_s$ ,  $v = 0.077c$ , and  $B = 10 G$ ;  $kT_e = 4.1$  MeV,  $R_0 = 10.4 R_s$ ,  $v = 0.091c$ ,  $B = 12 G$ ) yields similar emission region characteristics but is worse in matching the 43 GHz data. This is because the synchrotron spectrum is more strongly peaked than for a power-law electron population. As a result, the flare amplitude declines more rapidly at successively lower frequencies than is the case for power-law models (except for large choice of  $p$ ). Future simultaneous light curves with better time coverage are needed to confirm this results.

## 5.3. Criticism of the Hot Expanding Blob Model

Recently, Marrone et al. (2008) criticized the expanding blob model on the grounds that their measured ratio of 1.3 mm to 850  $\mu$ m flux during a flare on 2006 July 17 was higher than expected from the blob model, both in the optically thick precursors (where one would expect a spectral index of 5/2 rather than the measured value  $\beta = 0.1 \pm 0.5$ ), and in the ratio of the amplitudes of the flares at the two wavelengths. However, the continual variability at radio and millimetre means that there is a large uncertainty in determining the underlying background flux level for a particular flare, and we have determined that there are reasonable choices of the levels that renders flare profiles that are consistent with the plasmon framework. Fig. 27 demonstrates simultaneous fit to both the 1.3 mm and 850  $\mu$ m flux of the 2006 July 17 flares (see Figure 3 of Marrone et al.

2008) using the plasmon model. The parameters of the successful fits to the first flare peaking near 5.7 hr UT are  $p = 1$ ,  $R_0 = 0.52 R_s$ ,  $v = 0.011c$ , and  $B = 73 G$  whereas the parameters of the strong flare peaking near 7.5 hr UT are  $p = 0.5$ ,  $R_0 = 0.42 R_s$ ,  $v = 0.003c$ , and  $B = 75 G$ . These fits show clear evidence that a simple picture of plasmon model can easily be applied to previously published light curves in submillimeter wavelengths (see additional fits to light curves in Yusef-Zadeh et al. 2008).

The other criticism of Marrone et al. (2008) is that the model requires adiabatic expansion of the blobs at speeds  $\sim 0.03c$  much below than the canonical sound speed  $c/\sqrt{3}$  approaching the black hole that would be expected were the blobs filled with plasma and sitting in vacuum. Given that the blob diameters are in the range of several  $R_s$  they may well be located at 10 or more  $R_s$ , where the local sound speed would be  $\sim 0.1c$ . In any case, they may be embedded in the outer layers of an accretion flow where they would be only mildly overpressured with respect to their surroundings and the expansion time scale would be comparable to the buoyancy or orbital time scale.

#### 5.4. Alternative Models of Flare Emission

We discuss two models that attempt to explain the nature of the flare emission. One is an expanding hot plasma model in which the peak frequency of emission (e.g., the initial optically thin NIR flare) shifts toward lower frequencies (submillimeter, millimeter and then radio) as a self-absorbed synchrotron source cools adiabatically away from the acceleration site (Shklovskii 1960; van der Laan 1966; Yusef-Zadeh et al. 2006b, 2008). A variation of this model is a jet model in which the expansion speed of the plasma is relativistic and is collimated in the form of outflow. In the expanding blob model, polarized flare emission does not follow classical Faraday rotation and a frequency-dependent rotation measure (RM) is predicted (Yusef-Zadeh et al. 2007). The expanding blob picture considers hot plasma being launched from the disk. The cooling plasma is dominated by the magnetic pressure as the plasma escapes or remains bound to the system. The second model assumes that flares are hotspots that are orbiting within few  $R_s$  of the black hole (Broderick & Loeb 2006) where Doppler boosting and GR effects become important. The hot spot picture requires the hot plasma be embedded within the disk where the emission is dominated by the gas pressure in the disk before the hot spot plunges into the hole. Quasi-periodic flaring events are expected under the assumption that hot spots survive longer than the period of the last stable orbit. There are several issues that the hot spot model appears to be inconsistent with observations. One is the time delay between the peaks of flare emission which is not expected in this picture. It is possible that the optically thin and thick flare emission is not related to each other and that the hot spot model is applicable only to the NIR flare emission. However, recent measurements indicate time delay between the peaks of NIR/X-ray and submillimeter flare emission (Yusef-Zadeh et al. 2008; Marrone et al. 2008; Eckart et al. 2009).

Another difficulty with the hot spot model is the lack of evidence for power on the quasi-periodicity in NIR light curve (Do et al. 2008, Meyer et al. 2008). Claims of quasi-periodic variations in the NIR lightcurves were the motivating observation for the hotspot model, but the most thorough analysis of NIR lightcurve variability have not shown evidence for significant quasi-periodic power (Do et al. 2008; Meyer et al. 2008). Furthermore, MHD simulations of accreting gas indicate that hot spots can last less than an orbital time scale before they disperse (Hawley & Balbus 2002).

## 6. Conclusions

The main results of extensive observing campaign that took place in 2007 can be summarized as follows:

Simultaneous VLA and VLBA observations indicate that flare emission from Sgr A\* at 43 GHz arises from within the scattering size of Sgr A\* which is  $\sim 0.3 \times 0.7 \text{ mas}$  (Bower et al. 2004) or within the inner  $30 \times 70 R_s$  of Sgr A\*.

We show the evidence of varying spectral index values when weak and bright NIR flares are compared. In addition, the NIR flare statistics indicate that the probability of flare emission is proportional to the inverse of the flux density. Simulations of the histogram of such flares assuming uniform distribution of peak flare emission is consistent with observations. The significance of the probability of flare emission is inversely proportional to the flux of flare is not understood.

In addition to a powerful X-ray flare with a NIR counterpart and  $11.8 \mu\text{m}$  upper limit on 2007 April 4 that had been reported earlier by Porquet et al. (2008), Dodds-Edden et al. (2009), and Trap et al. (2009), we show evidence of three new X-ray flares with NIR counterparts. The origin of X-ray production is explained in the context of ICS employing the structure details of the Sgr A\* emitting region inferred from intrinsic size measurements. In this picture, the seed photons associated with flares in NIR wavelengths are upscattered by the sea of electrons that are responsible for the quiescent emission of the Sgr A\* in radio and submillimeter wavelengths. A prediction of this model is a time delay between the peaks of X-ray and NIR flare emission.

The comparison of the light curves at multiple wavelengths indicated time delays implying optically thick emission. We also argue a tantalizing radio flare three hours after the strongest NIR and X-ray flare detected on 2007 April 4. These measurements are consistent with an adiabatic expansion of hot plasma. Although these measurements weaken the hot spot model of flare emission, we can not distinguish whether there is jet activity associated with the observed time delays or the expansion of hot plasma that is bound to Sgr A\*.

### Acknowledgments:

This work is partially supported by the grant AST-0807400 from the National Science Foundation. Some of the data presented here were obtained from Mauna Kea observatories. We are grateful to the Hawai’ian people for permitting us to study the universe from this sacred summit. Research at the Caltech Submillimeter Observatory is supported by grant AST-0540882 from the National Science Foundation. Research grants are also given by Australian Research Council (DPO986386) and Macquarie University. The SMT is operated by the Arizona Radio Observatory (ARO), Steward Observatory, University of Arizona. The XMM-Newton project is an ESA Science Mission with instruments and contributions directly funded by ESA Member State and the USA (NASA).

## REFERENCES

Baars, J. W. M., Genzel, R., Pauliny-Toth, I. I. K., & Witzel, A. 1977, *A&A*, 61, 99

- Baars, J. W. M., Martin, R. N., Mangum, J. G., McMullin, J. P., & Peters, W. L. 1999, *PASP*, 111, 627
- Baganoff, F. K. 2003, in *Bulletin of the American Astronomical Society*, Vol. 35, *Bulletin of the American Astronomical Society*, 606–+
- Baganoff, F. K., Maeda, Y., Morris, M., Bautz, M. W., Brandt, W. N., Cui, W., Doty, J. P., Feigelson, E. D., Garmire, G. P., Pravdo, S. H., Ricker, G. R., & Townsley, L. K. 2003, *ApJ*, 591, 891
- Balick, B., & Brown, R. L. 1974, *ApJ*, 194, 265
- Bélanger, G., Goldwurm, A., Melia, F., Ferrando, P., Grosso, N., Porquet, D., Warwick, R., & Yusef-Zadeh, F. 2005, *ApJ*, 635, 1095
- Blandford, R. D., & Begelman, M. C. 1999, *MNRAS*, 303, L1
- Blundell, R. 2004, in *Proceedings of the 15th International Symposium on Space Terahertz Technology*, April 27-29, 2004, p. 3, 3–+
- Bower, G. C., Falcke, H., Herrnstein, R. M., Zhao, J.-H., Goss, W. M., & Backer, D. C. 2004, *Science*, 304, 704
- Broderick, A. E., & Loeb, A. 2006, *ApJ*, 636, L109
- Do, T., Ghez, A. M., Morris, M. R., Yelda, S., Lu, J. R., Hornstein, S. D., & Matthews, K. 2008, *Journal of Physics Conference Series*, 131, 012003
- Dodds-Eden, K., Porquet, D., Trap, G., Quataert, E., Haubois, X., Gillessen, S., Grosso, N., Pantin, E., Falcke, H., Rouan, D., Genzel, R., Hasinger, G., Goldwurm, A., Yusef-Zadeh, F., Clenet, Y., Trippe, S., Lagage, P. ., Bartko, H., Eisenhauer, F., Ott, T., Paumard, T., Perrin, G., Yuan, F., Fritz, T. K., & Mascetti, L. 2009, *ArXiv e-prints*
- Doeleman, S. S., Weintraub, J., Rogers, A. E. E., Plambeck, R., Freund, R., Tilanus, R. P. J., Friberg, P., Ziurys, L. M., Moran, J. M., Corey, B., Young, K. H., Smythe, D. L., Titus, M., Marrone, D. P., Cappallo, R. J., Bock, D. C.-J., Bower, G. C., Chamberlin, R., Davis, G. R., Krichbaum, T. P., Lamb, J., Maness, H., Niell, A. E., Roy, A., Strittmatter, P., Werthimer, D., Whitney, A. R., & Woody, D. 2008, *Nature*, 455, 78
- Eckart, A., Baganoff, F. K., Morris, M., Bautz, M. W., Brandt, W. N., Garmire, G. P., Genzel, R., Ott, T., Ricker, G. R., Straubmeier, C., Viehmann, T., Schödel, R., Bower, G. C., & Goldston, J. E. 2004, *A&A*, 427, 1
- Eckart, A., Baganoff, F. K., Morris, M. R., Kunneriath, D., Zamaninasab, M., Witzel, G., Schödel, R., Garc´ıa-Mar´ın, M., Meyer, L., Bower, G. C., Marrone, D., Bautz, M. W., Brandt, W. N., Garmire, G. P., Ricker, G. R., Straubmeier, C., Roberts, D. A., Muzic, K., Mauerhan, J., & Zensus, A. 2009, *ArXiv e-prints*
- Eckart, A., Baganoff, F. K., Schödel, R., Morris, M., Genzel, R., Bower, G. C., Marrone, D., Moran, J. M., Viehmann, T., Bautz, M. W., Brandt, W. N., Garmire, G. P., Ott, T., Trippe, S., Ricker, G. R., Straubmeier, C., Roberts, D. A., Yusef-Zadeh, F., Zhao, J. H., & Rao, R. 2006a, *A&A*, 450, 535

- Eckart, A., Schödel, R., Garc´ıa-Mar´ın, M., Witzel, G., Weiss, A., Baganoff, F. K., Morris, M. R., Bertram, T., DovVciak, M., Duschl, W. J., Karas, V., König, S., Krichbaum, T. P., Krips, M., Kunneriath, D., Lu, R.-S., Markoff, S., Mauerhan, J., Meyer, L., Moutaka, J., MuVzić, K., Najarro, F., Pott, J.-U., Schuster, K. F., Sjouwerman, L. O., Straubmeier, C., Thum, C., Vogel, S. N., Wiesemeyer, H., Zamaninasab, M., & Zensus, J. A. 2008, *A&A*, 492, 337
- Eckart, A., Schödel, R., Meyer, L., Trippe, S., Ott, T., & Genzel, R. 2006b, *A&A*, 455, 1
- Eisenhauer, F., Genzel, R., Alexander, T., Abuter, R., Paumard, T., Ott, T., Gilbert, A., Gillessen, S., Horrobin, M., Trippe, S., Bonnet, H., Dumas, C., Hubin, N., Kaufer, A., Kissler-Patig, M., Monnet, G., Ströbele, S., Szeifert, T., Eckart, A., Schödel, R., & Zucker, S. 2005, *ApJ*, 628, 246
- Falcke, H., Goss, W. M., Matsuo, H., Teuben, P., Zhao, J.-H., & Zylka, R. 1998, *ApJ*, 499, 731
- Falcke, H., & Markoff, S. 2000, *A&A*, 362, 113
- Falcke, H., Markoff, S., & Bower, G. C. 2009, *A&A*, 496, 77
- Genzel, R. 2000, *ArXiv Astrophysics e-prints*
- Genzel, R., Schödel, R., Ott, T., Eckart, A., Alexander, T., Lacombe, F., Rouan, D., & Aschenbach, B. 2003, *Nature*, 425, 934
- Genzel, R., & Townes, C. H. 1987, *ARA&A*, 25, 377
- Ghez, A. M., Becklin, E., Duchjne, G., Hornstein, S., Morris, M., Salim, S., & Tanner, A. 2003, *Astronomische Nachrichten Supplement*, 324, 527
- Ghez, A. M., Salim, S., Hornstein, S. D., Tanner, A., Lu, J. R., Morris, M., Becklin, E. E., & Duchêne, G. 2005, *ApJ*, 620, 744
- Ghez, A. M., Salim, S., Weinberg, N. N., Lu, J. R., Do, T., Dunn, J. K., Matthews, K., Morris, M. R., Yelda, S., Becklin, E. E., Kremenek, T., Milosavljevic, M., & Naiman, J. 2008, *ApJ*, 689, 1044
- Ghez, A. M., Wright, S. A., Matthews, K., Thompson, D., Le Mignant, D., Tanner, A., Hornstein, S. D., Morris, M., Becklin, E. E., & Soifer, B. T. 2004, *ApJ*, 601, L159
- Gillessen, S., Eisenhauer, F., Quataert, E., Genzel, R., Paumard, T., Trippe, S., Ott, T., Abuter, R., Eckart, A., Lagage, P. O., Lehnert, M. D., Tacconi, L. J., & Martins, F. 2006, *ApJ*, 640, L163
- Gillessen, S., Eisenhauer, F., Trippe, S., Alexander, T., Genzel, R., Martins, F., & Ott, T. 2009, *ApJ*, 692, 1075
- Goldston, J. E., Quataert, E., & Igumenshchev, I. V. 2005, *ApJ*, 621, 785
- Goldwurm, A., Brion, E., Goldoni, P., Ferrando, P., Daigne, F., Decourchelle, A., Warwick, R. S., & Predehl, P. 2003, *ApJ*, 584, 751
- Hawley, J. F., & Balbus, S. A. 2002, *ApJ*, 573, 738

- Hornstein, S. D., Matthews, K., Ghez, A. M., Lu, J. R., Morris, M., Becklin, E. E., Rafelski, M., & Baganoff, F. K. 2007, *ApJ*, 667, 900
- Kreysa, E. 1990, in *Liege International Astrophysical Colloquia*, Vol. 29, *Liege International Astrophysical Colloquia*, ed. B. Kaldeich, 265–270
- Li, H., Dowell, C. D., Kirby, L., Novak, G., & Vaillancourt, J. E. 2008, *Appl. Opt.*, 47, 422
- Liu, S., & Melia, F. 2001, *ApJ*, 561, L77
- . 2002, *ApJ*, 566, L77
- Liu, S., Melia, F., & Petrosian, V. 2006, *ApJ*, 636, 798
- Liu, S., Petrosian, V., & Melia, F. 2004, *ApJ*, 611, L101
- Loeb, A., & Waxman, E. 2007, *Journal of Cosmology and Astro-Particle Physics*, 3, 11
- Marrone, D. P., Baganoff, F. K., Morris, M. R., Moran, J. M., Ghez, A. M., Hornstein, S. D., Dowell, C. D., Muñoz, D. J., Bautz, M. W., Ricker, G. R., Brandt, W. N., Garmire, G. P., Lu, J. R., Matthews, K., Zhao, J.-H., Rao, R., & Bower, G. C. 2008, *ApJ*, 682, 373
- Marrone, D. P., & Rao, R. 2008, in *Presented at the Society of Photo-Optical Instrumentation Engineers (SPIE) Conference*, Vol. 7020, *Society of Photo-Optical Instrumentation Engineers (SPIE) Conference Series*
- Melia, F. 1992, *ApJ*, 387, L25
- Melia, F. 2002, in *Bulletin of the American Astronomical Society*, Vol. 34, *Bulletin of the American Astronomical Society*, 951–+
- Melia, F., & Falcke, H. 2001, *ARA&A*, 39, 309
- Meyer, L., Do, T., Ghez, A., Morris, M. R., Witzel, G., Eckart, A., Bélanger, G., & Schödel, R. 2008, *ApJ*, 688, L17
- Moneti, A., Stolovy, S., Blommaert, J. A. D. L., Figer, D. F., & Najarro, F. 2001, *A&A*, 366, 106
- Narayan, R., Mahadevan, R., Grindlay, J. E., Popham, R. G., & Gammie, C. 1998, *ApJ*, 492, 554
- Porquet, D., Grosso, N., Predehl, P., Hasinger, G., Yusef-Zadeh, F., Aschenbach, B., Trap, G., Melia, F., Warwick, R. S., Goldwurm, A., Bélanger, G., Tanaka, Y., Genzel, R., Dodds-Eden, K., Sakano, M., & Ferrando, P. 2008, *A&A*, 488, 549
- Porquet, D., Predehl, P., Aschenbach, B., Grosso, N., Goldwurm, A., Goldoni, P., Warwick, R. S., & Decourchelle, A. 2003, *A&A*, 407, L17
- Reid, M. J., & Brunthaler, A. 2004, *ApJ*, 616, 872
- Scargle, J. D. 1982, *ApJ*, 263, 835
- Schödel, R., Ott, T., Genzel, R., Hofmann, R., Lehnert, M., Eckart, A., Mouawad, N., Alexander, T., Reid, M. J., Lenzen, R., Hartung, M., Lacombe, F., Rouan, D., Gendron, E., Rousset, G., Lagrange, A.-M., Brandner, W., Ageorges, N., Lidman, C., Moorwood, A. F. M., Spyromilio, J., Hubin, N., & Menten, K. M. 2002, *Nature*, 419, 694

- Shklovskii, I. S. 1960, *Soviet Astronomy*, 4, 355
- Trap, G., Goldwurm, A., Terrier, R., Dodds-Eden, K., Gillessen, S., Genzel, R., Pautin, E., Lagage, P., Ferrando, P., Belanger, G., Porquet, D., Grosso, N., Yusef-Zadeh, F., & Melia, F. 2009, *Advances in Space Research*, submitted
- van der Laan, H. 1966, *Nature*, 211, 1131
- Yuan, F., Markoff, S., & Falcke, H. 2002, *A&A*, 383, 854
- Yuan, F., Quataert, E., & Narayan, R. 2003, *ApJ*, 598, 301
- Yusef-Zadeh, F., Bushouse, H., Dowell, C. D., Wardle, M., Roberts, D., Heinke, C., Bower, G. C., Vila-Vilaró, B., Shapiro, S., Goldwurm, A., & Bélanger, G. 2006a, *ApJ*, 644, 198
- Yusef-Zadeh, F., Roberts, D., Wardle, M., Heinke, C. O., & Bower, G. C. 2006b, *ApJ*, 650, 189
- Yusef-Zadeh, F., Wardle, M., Heinke, C., Dowell, C. D., Roberts, D., Baganoff, F. K., & Cotton, W. 2008, *ApJ*, 682, 361
- Zylka, R., Mezger, P. G., & Lesch, H. 1992, *A&A*, 261, 119



Table 1. Spectral Index Distribution Using NICMOS

Event	$F(1.45\mu\text{m} \pm \sigma)$	$F(1.70\mu\text{m} \pm \sigma)$	$\beta \pm \sigma$
5A	$8.55 \pm 0.4$	$9.61 \pm 0.4$	$0.73 \pm 0.39$
2A	$6.77 \pm 0.6$	$7.92 \pm 0.5$	$0.97 \pm 0.68$
2C	$4.54 \pm 0.1$	$6.54 \pm 0.7$	$2.29 \pm 0.27$
4A	$4.77 \pm 0.1$	$6.14 \pm 0.3$	$1.59 \pm 0.33$
5B	$2.31 \pm 0.5$	$3.62 \pm 0.4$	$2.82 \pm 1.51$
7A	$2.85 \pm 0.3$	$3.63 \pm 0.2$	$1.52 \pm 0.74$

Table 2. Measured Time Lags with  $1\text{-}\sigma$  Errors

Date	Time Delay					
2007	84-43	134-146	450-230	1.70-230	3.8-43	3.8-X-rays
April	(GHz-GHz)	(GHz-GHz)	( $\mu\text{m}$ -GHz)	( $\mu\text{m}$ -GHz)	( $\mu\text{m}$ -GHz)	( $\mu\text{m}$ -2-10keV)
	(hr)	(min)	(hr)	(hr)	(hr)	(min)
1	—	—	$0.24(-0.29, +1.12)$	—	—	—
2	$1.02(-0.31, +0.16)$	—	—	—	—	—
3	—	—	$1.32(-0.63, +0.33)$	—	—	—
4	—	$3(-8.0, +3.4)$	—	—	$3.05(-0.19, +0.1)$	$0.5(-6.5, +7)$
5	—	—	—	$2.64 (-0.67, +0.5)$	—	—

## Observational Schedule: The April 2007 Campaign

	April 1	April 2	April 3	April 4	April 5	April 6	April 7	April 10	April 11
HST 1.7, 1.4 $\mu$ m	■	■	■	■	■	■	■		
XMM 2-12 keV	■	■	■	■					
CSO 350, 600, 850 $\mu$ m	■	■	■	■	■	■			
VLA 43, 22 GHz	■	■	■	■					
SMA 230 GHz	■		■	■	■				
CARMA 240 GHz		■	■	■	■				
IRAM 240 GHz	■	■	■	■					
NMA 90, 130 GHz	■	■	■	■					
SMT 250 GHz	■	■	■	■	■				
VLT 2.2, 3.8, 11.8 $\mu$ m,	■	■	■	■	■	■			
GMRT 0.3, 0.6, 1.3GHz		■	■	■					
INTEGRAL 20-100 keV	■	■	■	■					
VLBA 14, 22,43 GHz	■	■			■			■	■

Fig. 1.—: A schematic diagram showing 13 telescopes joining the 2007 April campaign. The width of individual observing period is not scaled.

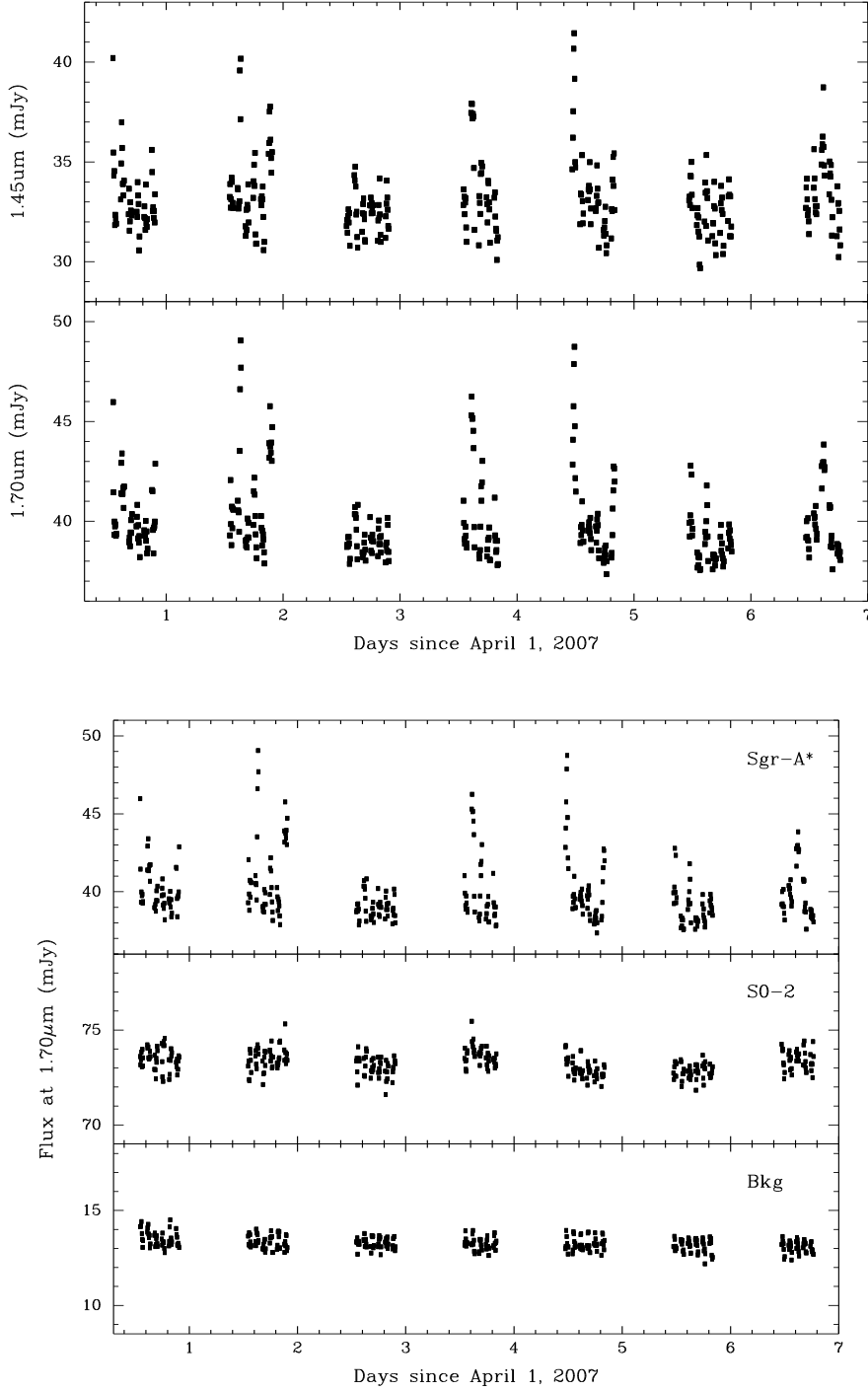


Fig. 2.—: (a) The light curves of Sgr A\* at  $1.45\mu\text{m}$  and  $1.70\mu\text{m}$  for the seven windows of HST observations on 2007 April 1–7. No background flux is removed from these plots. (b) The HST  $1.70\mu\text{m}$  light curves of Sgr A\*, the star S0-2, and a region of background emission. The constancy of the S0-2 and background light curves strongly suggest that the variability of Sgr A\* emission is intrinsic to Sgr A\*.

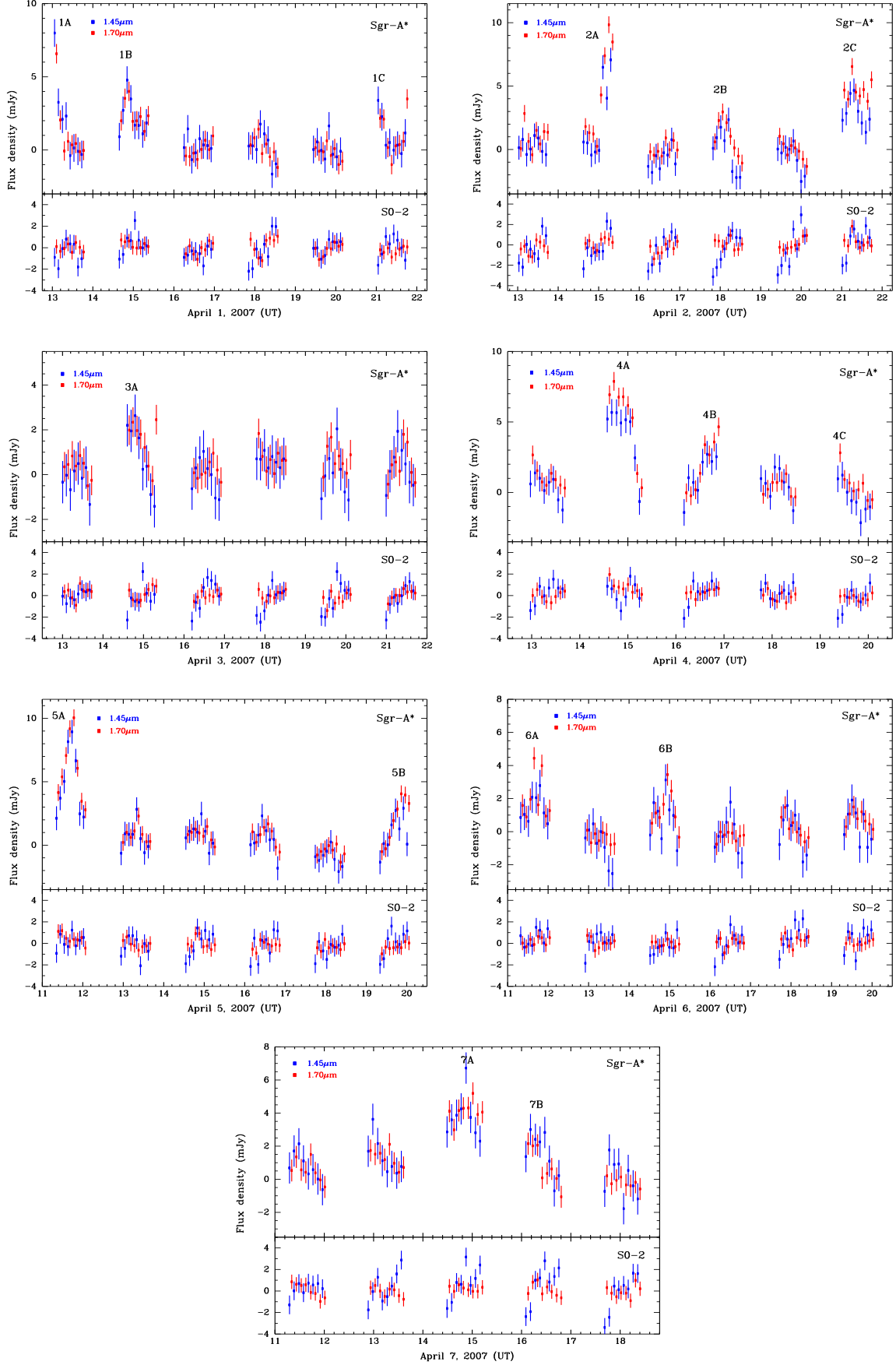


Fig. 3.— The background subtracted light curves of Sgr A\* and S0-2 for each of the seven HST observing windows, with flare events labeled. The data points at 1.70 and 1.45  $\mu\text{m}$  are sampled at 144 sec intervals.

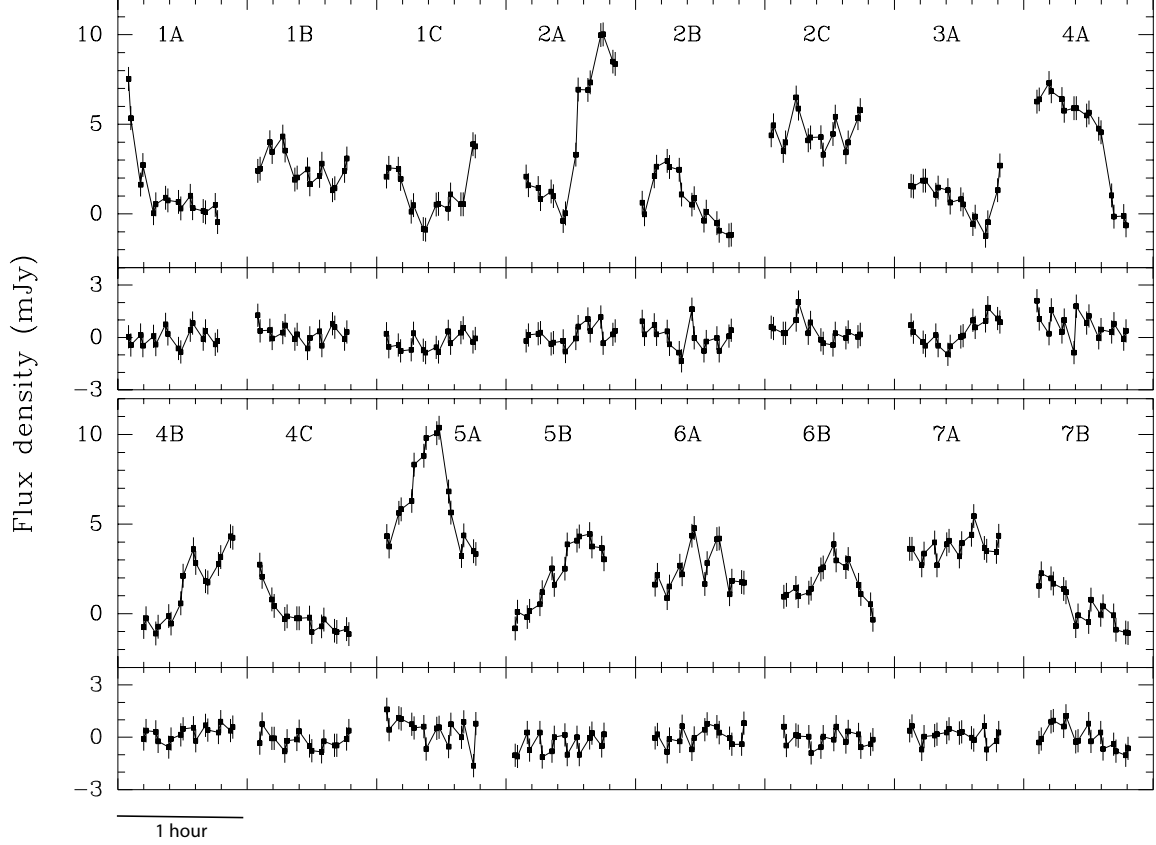


Fig. 4.— This plot shows all the 64-sec sampled data for the 16 periods that flares are identified. The 16 periods are stacked on the top and bottom panels. The x-axis is the elapsed time - each flare episode occupies a 45-minute slice within the 8-hour axis. Each flare event is labeled, as defined in Figure 3, The Sgr A\* and S0-2 light curves are on the upper and lower portion of the panel. The data show only the  $1.70\mu\text{m}$  photometry sampled at intervals of 64 sec but the light curves for each flare are laid side by side.

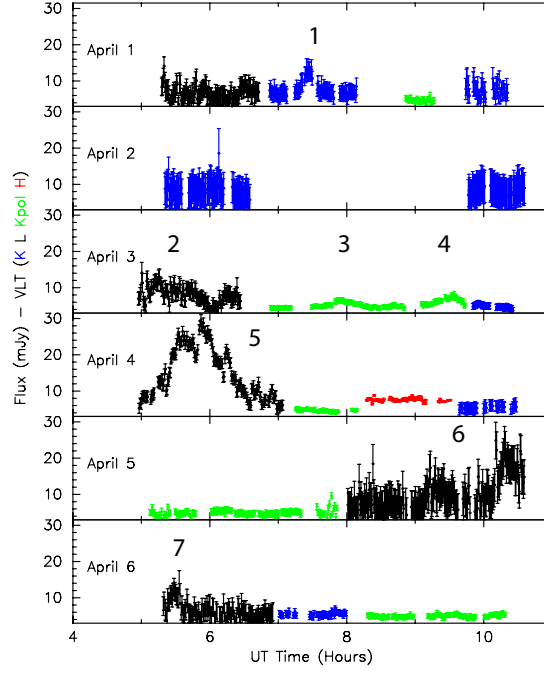


Fig. 5.—: Light curves of SgrA\* for April 1-6 at H ( $1.66 \mu\text{m}$ ), in red,  $K_s$  ( $2.12 \mu\text{m}$ ), in blue,  $K_s$  in polarimetric mode in blue and  $L'$  ( $3.8 \mu\text{m}$ ), in black, bands. are taken from Dodds-Eden et al. (2009). There are a total of seven periods of flaring activity reported in these observations. The brightest flares occurred on 2007, April 4 and April 5.

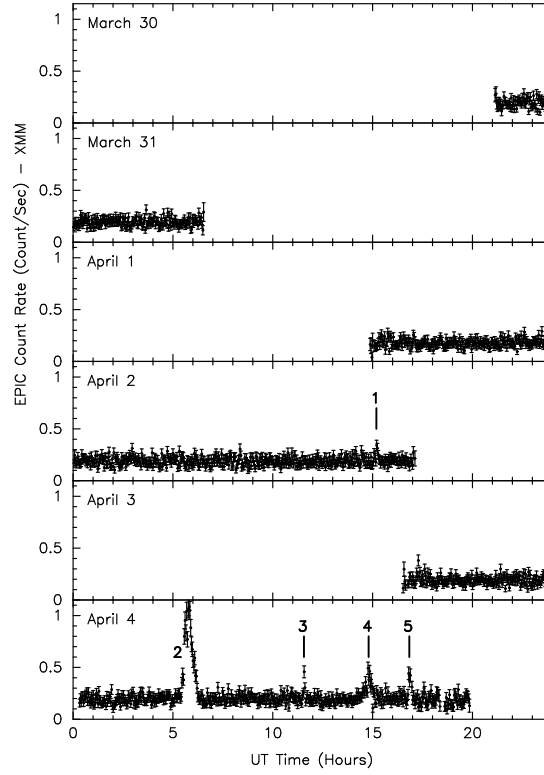


Fig. 6.—: Light curves of all the X-ray data taken with the XMM-Newton during the 2007 April observing campaign (Porquet et al. 2008). The data are averaged over a 144sec sampling. Five X-ray flares are detected, four of which had simultaneous coverage with the VLT and HST and showed NIR counterparts.

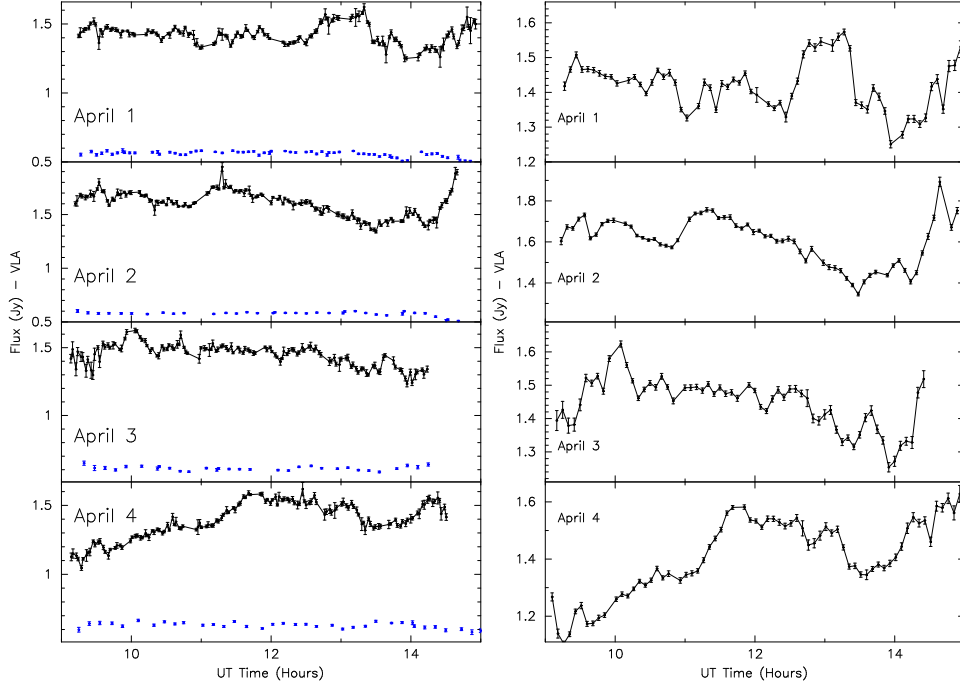


Fig. 7.—: (a - Left) Light curves of Sgr A\* and the calibrator 17444-31166 at 43 GHz data obtained with VLA observations taken during 2007, April 1-4. The sampling time is 87s for Sgr A\* and 90 sec for the calibrator at the bottom of each panel. The Sgr A\*  $uv$  data is restricted to  $>100k\lambda$  in order to suppress the contribution of extended emission. (b - Right) Similar to (a) except that only the light curves of Sgr A\* are shown with a sampling time of 300 sec.

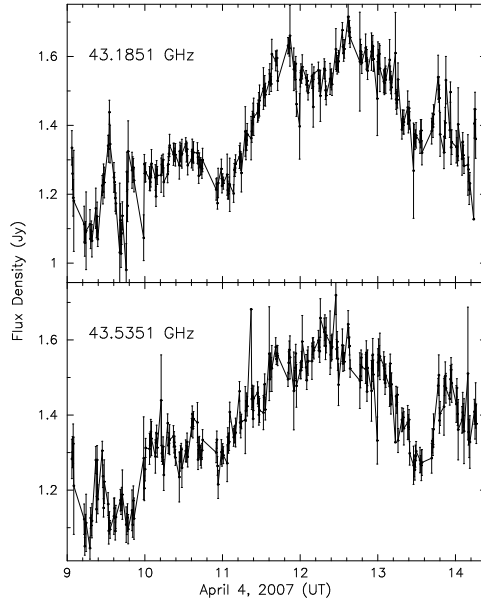


Fig. 7.—: (c) The light curves of Sgr A\* on 2007, April 4 are shown in the top and bottom panels at 43.185 GHz and 43.535 GHz, respectively. The light curves are shown with a 30s sampling time. The data points with large error bars correspond to a small number of data points in a given sample. The data corresponding to minimum and maximum  $uv$  baselines are selected between 110 and 125  $k\lambda$ .

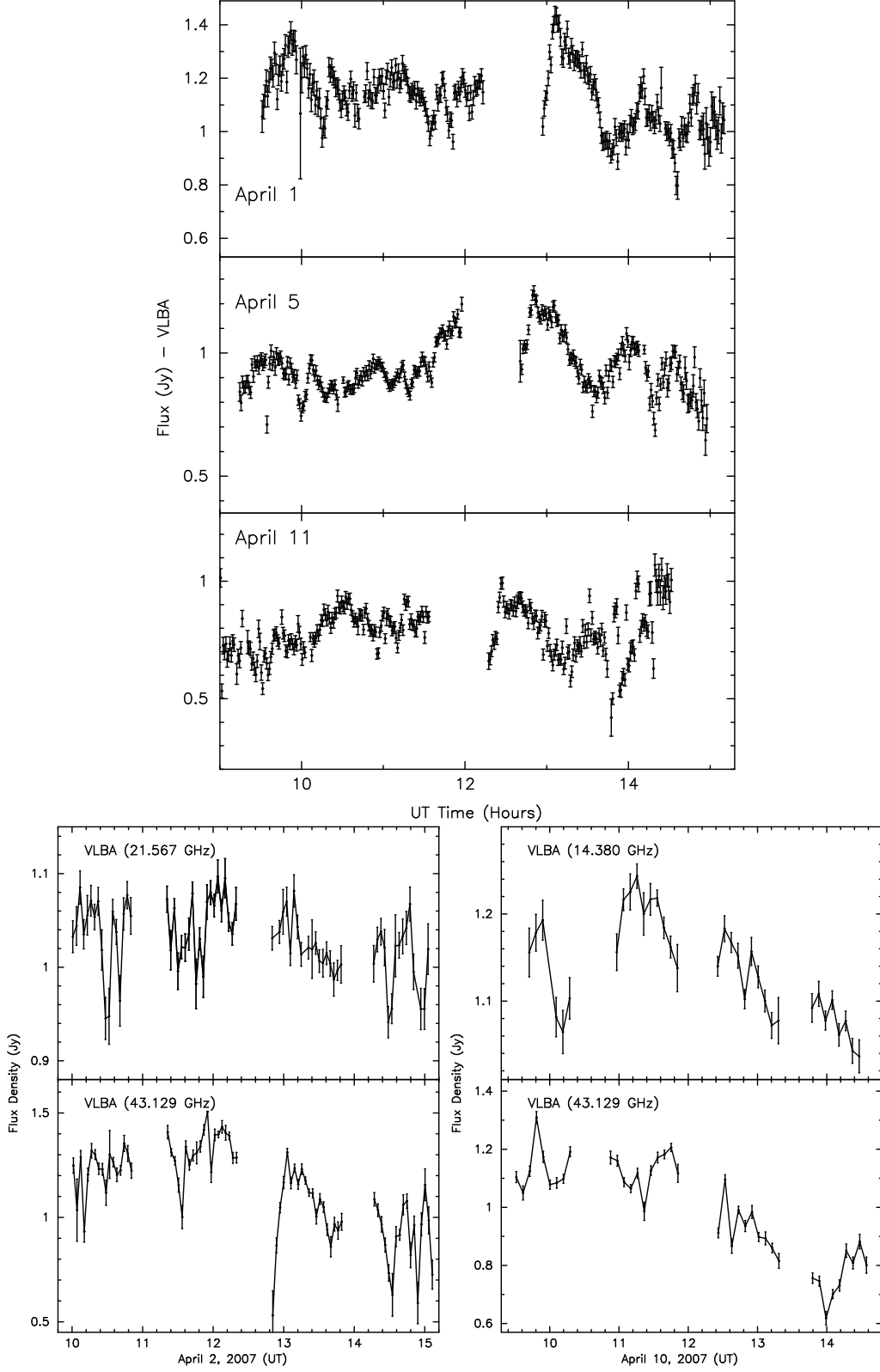


Fig. 8.— (a - Top ) Light curves of Sgr A\* on 2007, April 1, 5 and 11 using VLBA at 43.22 GHz. The sampling time is 60 sec. (b - Bottom Left) The light curve of Sgr A\* observed with VLBA on April 2, 2007 at 22 and 43 GHz. The sampling time is 300 sec. (c - Bottom Right ) The light curve of Sgr A\* observed with VLBA on April 10, 2007 at 14 and 43 GHz. The sampling time is 300 sec.



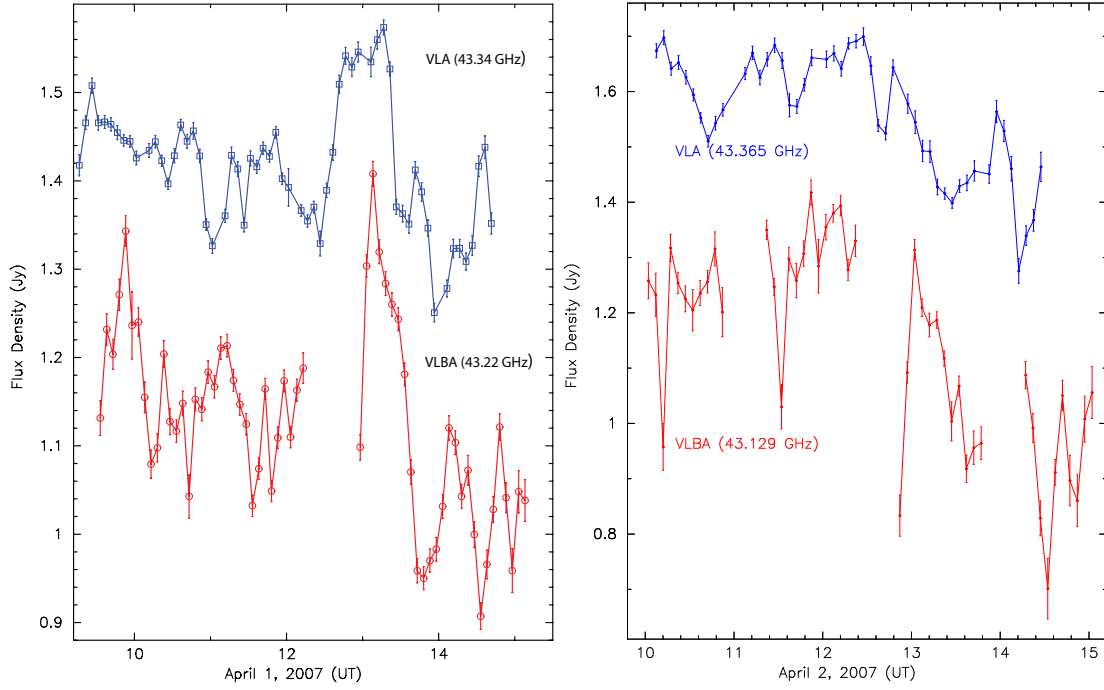


Fig. 9.—: (a - Left) The light curve of Sgr A\* observed with VLA and VLBA on April 1, 2007. The sampling time is 300 sec. The center frequencies of the VLA and VLBA light curves correspond to 43.34 GHz 43.22 GHz, respectively. The selected VLA  $uv$  data is  $>90k\lambda$ . (b - Right) Similar to (a) except that the observations are carried out on April 2 at 43 GHz. VLBA Observations on April 1 (bottom panel) are sampled continuously those made on April 2. VLBA plots are shown in red (bottom) whereas VLA plots are shown in blue (top).

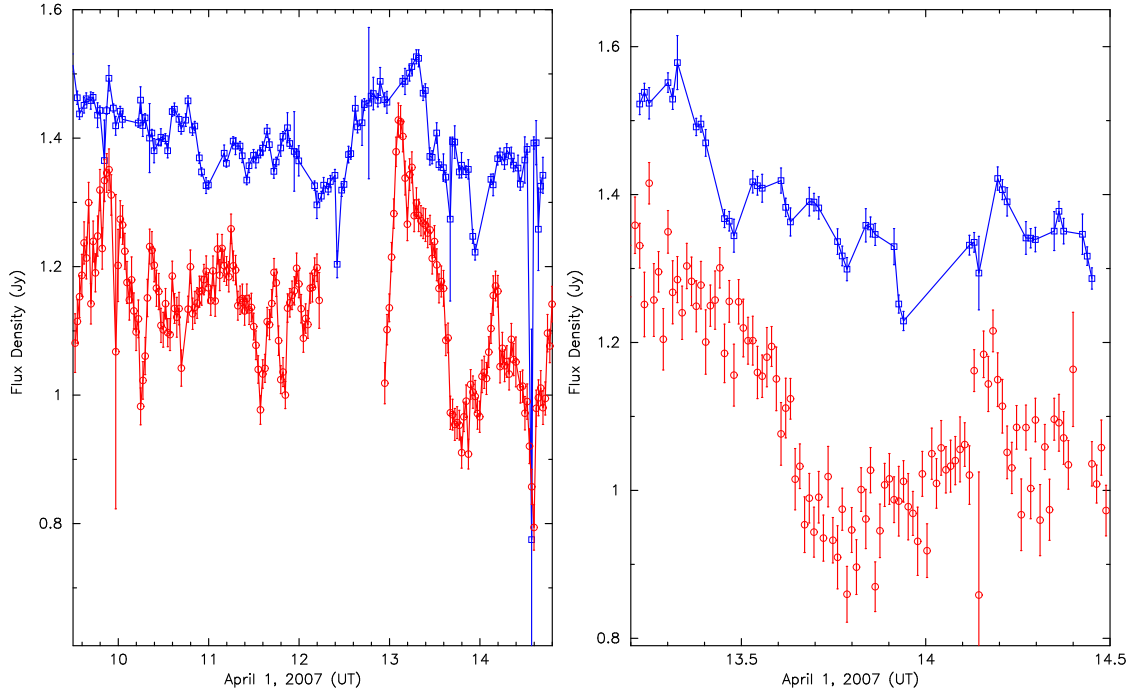


Fig. 9.—: (*c - Left*) The light curve is similar to (a) except that the sampling time is 90 sec for data taken with the VLA and VLBA, respectively. (*d - Right*) Similar to (c) except a zoomed time interval near 14h UT is shown with a sampling time of 46s for both light curves. The VLA  $uv$  data corresponds to IF2 at 43.3649 GHz using  $uv$  data  $> 80k\lambda$ . The selected VLBA  $uv$  data is  $< 10^5k\lambda$  at 43.217 GHz. The VLA flux measurements (blue) are higher than the VLBA measurements (red), as shown in (a), (c) and (d).

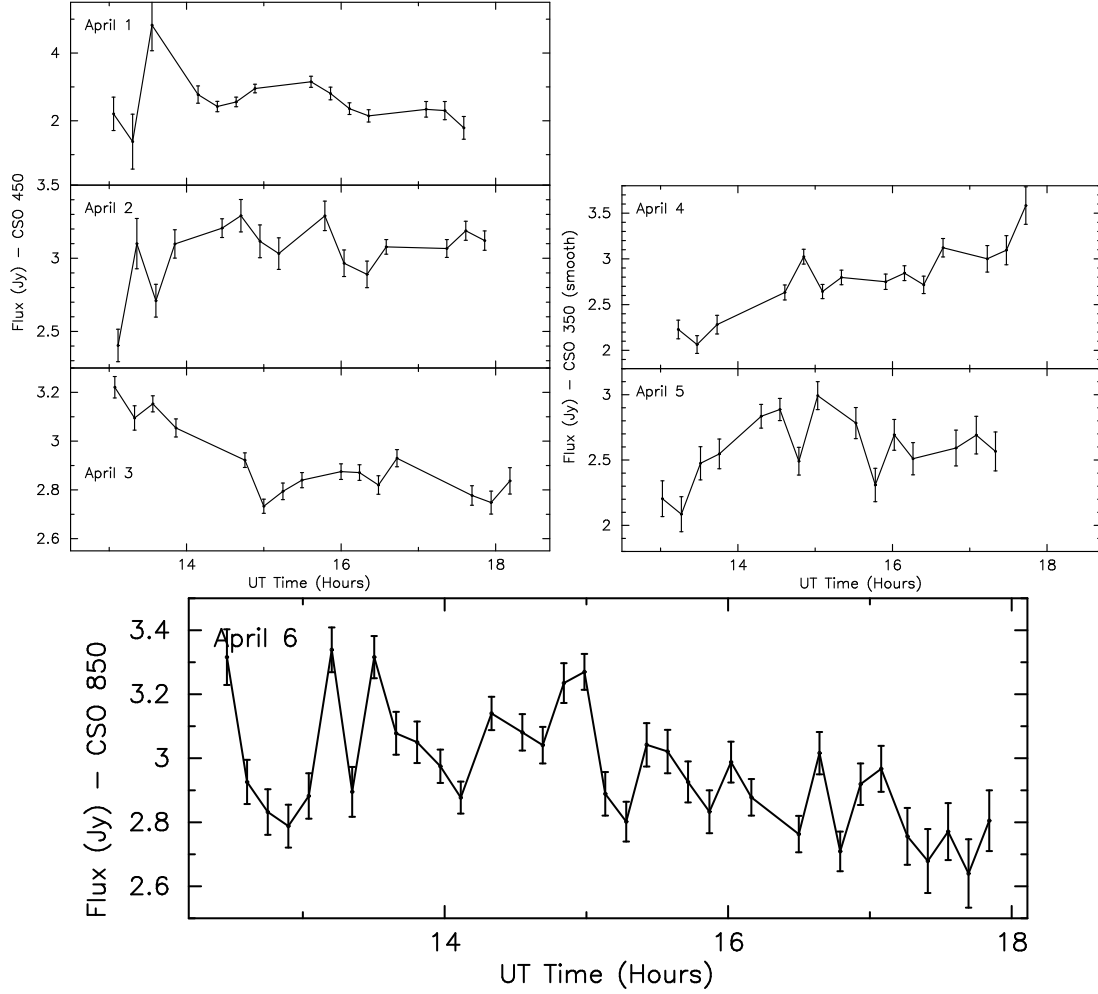


Fig. 10.—: (a) Light curves of Sgr A\* at  $450\mu\text{m}$  based on CSO observations on 2007, April 1-3 with a sampling time of 15 minutes. (b) Similar to (a) except at  $350\mu\text{m}$  on 2007, April 4-5 with a sampling time of 15 minutes. (c) Similar to (a) except at  $850\mu\text{m}$  on 2007, April 6 using a sampling time of 10 minutes.

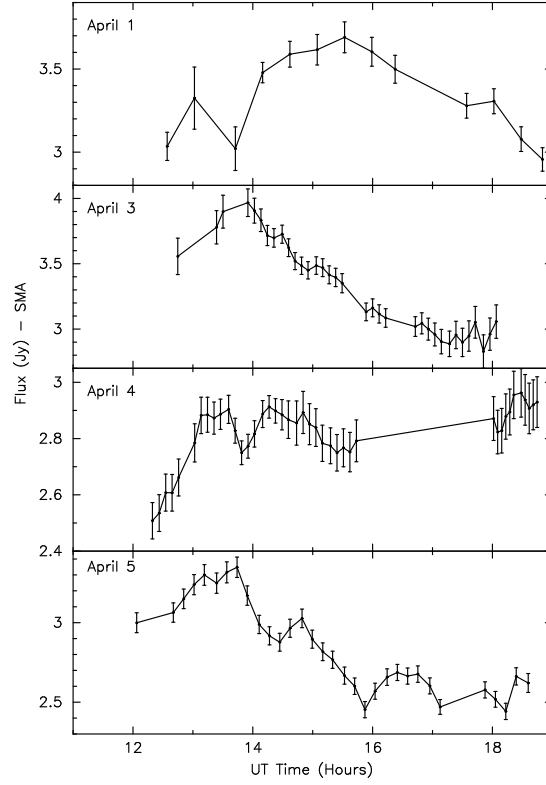


Fig. 11.—: Light curves of Sgr A\* at 230 GHz using SMA on 2007 April 1, and 3-5. The sampling times are 27 min, 6.5 min, 8 min and 10 min for the April 1, 3, 4 and 5 light curves, respectively.

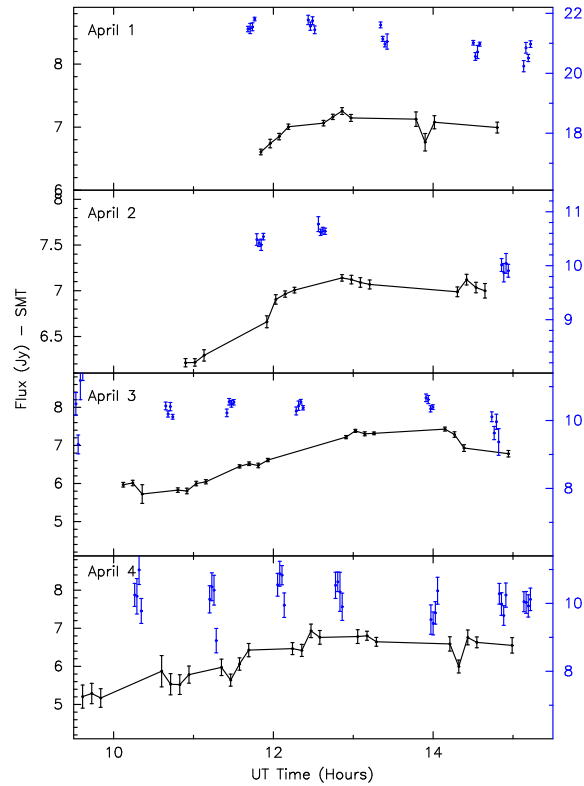


Fig. 12.—: Light curves of Sgr A\* and the calibrator G34.3 and 1757-240 (blue) at 230 GHz using SMT on 2007 April 1 and April 2-4, respectively, with a sampling time of  $\sim 7$  minutes.

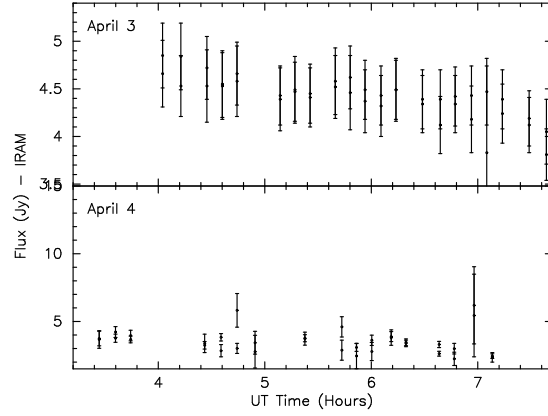


Fig. 13.—: Light curves of Sgr A\* at 240 GHz (1.25mm) taken with IRAM on 2007, April 3-4 with sampling time of  $\sim 10$  minutes. For each time sample, there are two data points estimating the flux of SgrA\* from repeated pointing measurements.

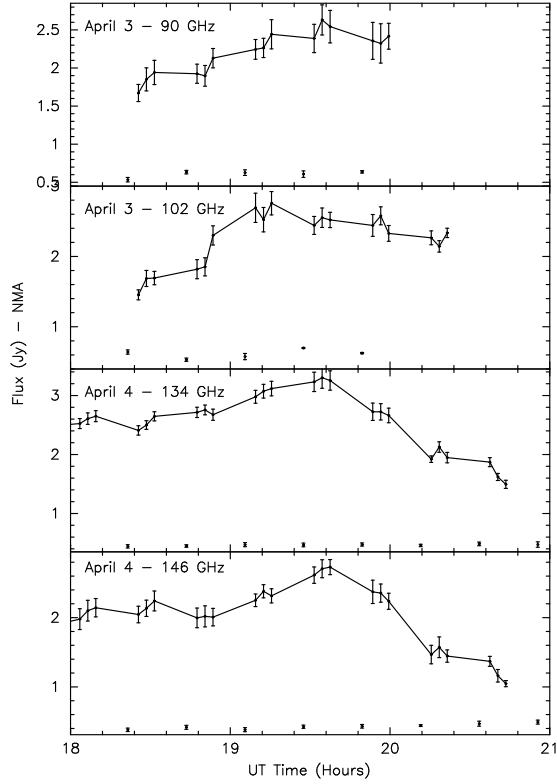


Fig. 14.—: Light curves of Sgr A\* taken with the NMA. The top panels show the light curves of Sgr A\* at 90 GHz and 102 GHz on April 3 whereas the bottom two panels show simultaneous light curves at 2.23mm (134 GHz) and 146 GHz on 2007, April 4. The flux of the calibrator 1744-312 is shown at the bottom of each panel. The sampling time is 3 minutes.

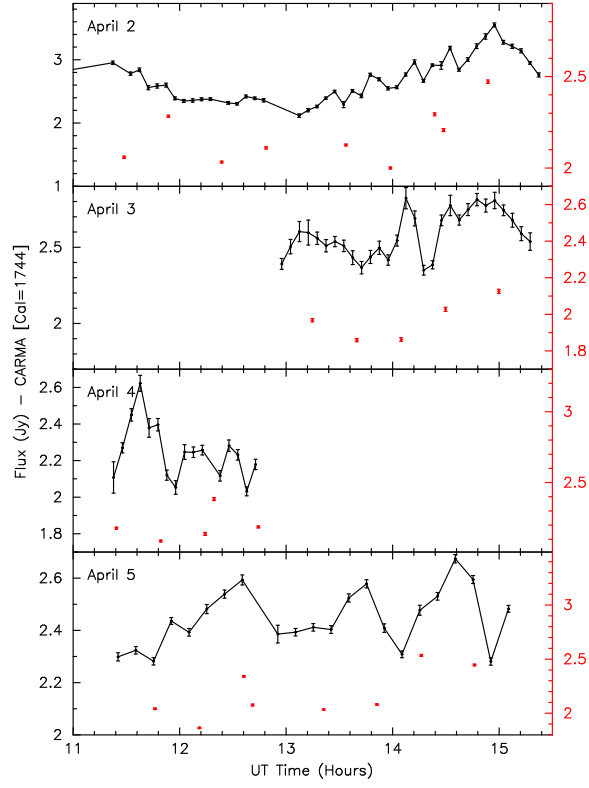


Fig. 15.—: Light curves of Sgr A\* and the calibrator 1730-130 obtained with CARMA at 90 GHz with a sampling time of 300 sec on 2007, April 2-5. The  $uv$  data  $> 20\text{k}\lambda$  are used to make the Sgr A\* light curves.

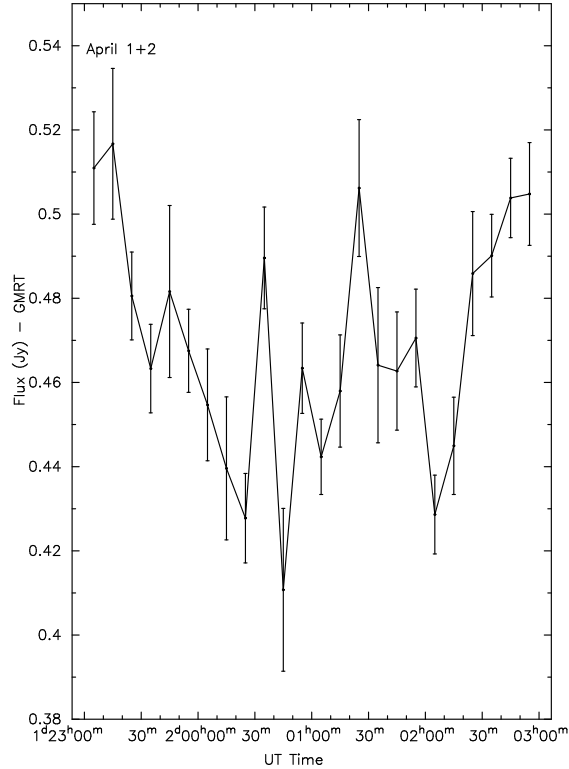


Fig. 16.—: The light curve of Sgr A\* at 23.3cm (1.287 GHz) using GMRT with a sampling time of 600 sec. The  $uv$  data has been restricted to  $> 80\text{k}\lambda$  in order to construct this light curve.

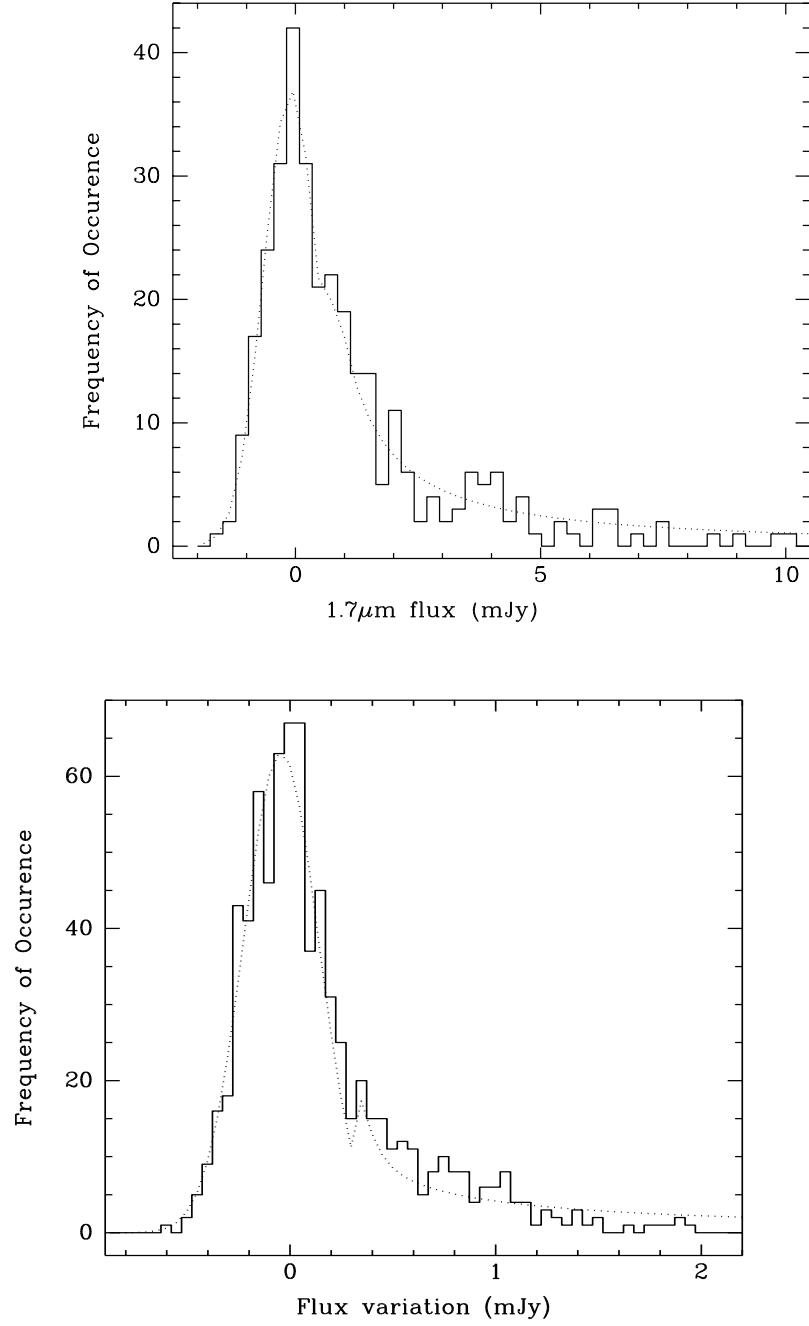


Fig. 17.—: (a) A histogram plot of the detected signals and the noise at  $1.70\mu\text{m}$  as well as the simultaneous single Gaussian fit and power law fits to both the noise and the flares. The dotted lines show the Gaussian and power law fits. (b) Similar to (a) expect that the 2004 histogram of flare activity (Yusef-Zadeh et al. 2006) is plotted at  $1.60\mu\text{m}$ .

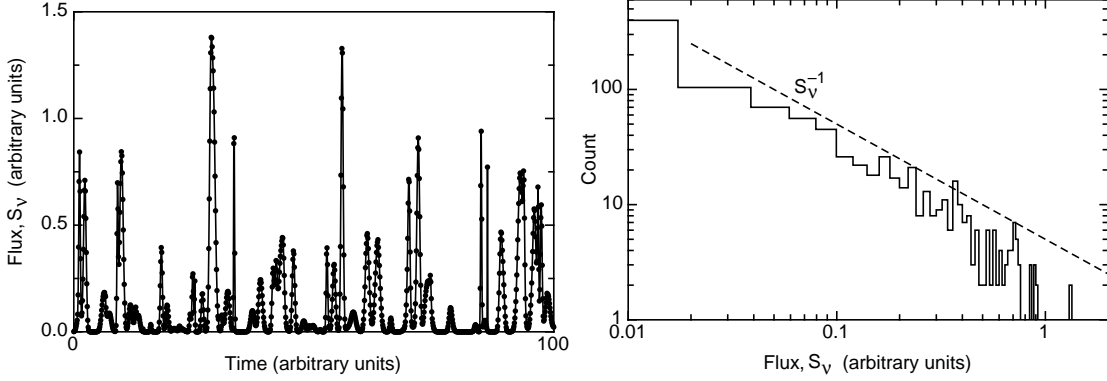


Fig. 18.—: (a) (*Left*) A synthetic light curve constructed from the sum of 100 Gaussian profiles with peak positions and, standard deviations drawn uniformly between -1.5 to 101.5 and 0 to 0.5 time units respectively; the probability distribution of the peak fluxes are distributed as  $1/(\text{peak flux})$  between 0.01 and 1 flux units. (b) (*Right*) Distribution of uniformly sampled flux values in the simulated flares. The dashed line indicates a slope of  $1/S_v$ .

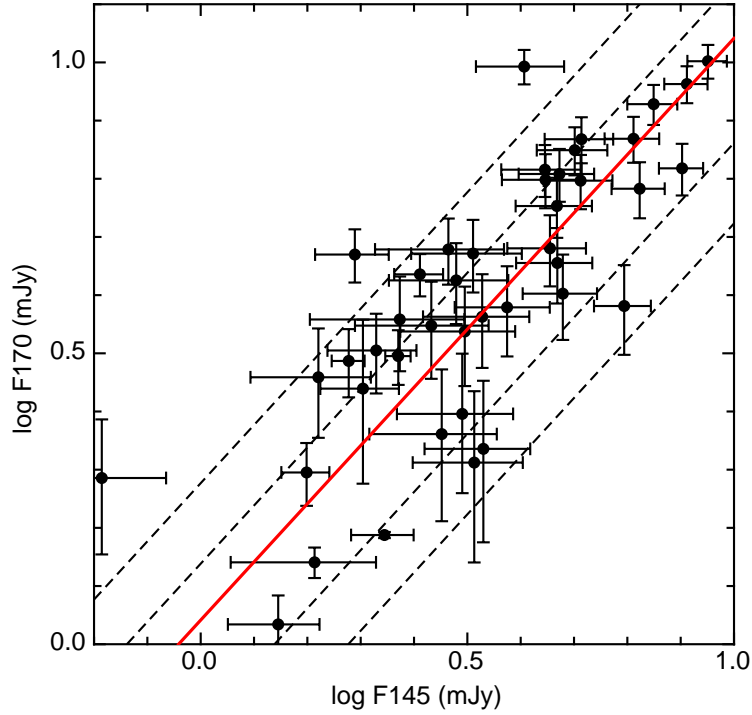


Fig. 19.—: A log-log plot of NIR fluxes in the F170 and F145 filters of NICMOS at  $1.70\mu\text{m}$  and  $1.45\mu\text{m}$ , respectively. The thick line in red shows the spectral index  $\beta=0.6$ . The thin dotted lines to the right and left of the  $\beta = 0.6$  line correspond to  $\beta = -2, -4$  and  $\beta = +2, +4$ , respectively.



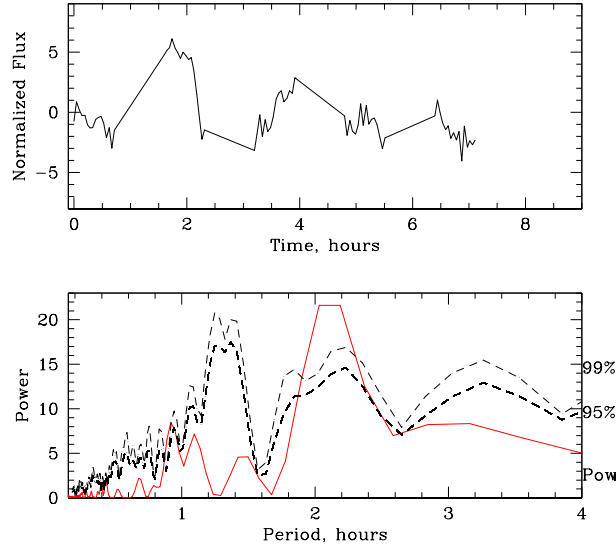


Fig. 20.—: The top and bottom boxes show the light curve of 2007, April 4 based on HST observations and the corresponding power spectrum of the residual flux of Sgr A\*, respectively. The dashed lines show the significance of the power spectrum at 95% and 99% confidence levels.

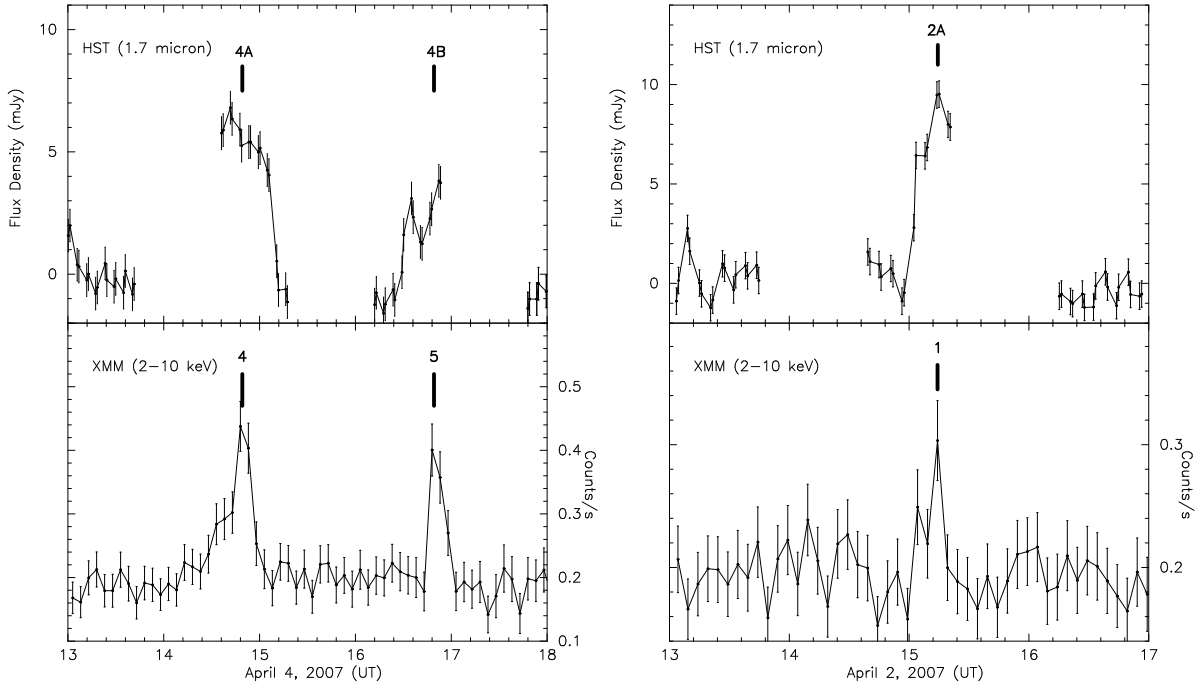


Fig. 21.—: (a - Left) The top panel shows the light curves of two near-IR flares identified as 4A and 4B measured with NICMOS on 2007, April 4 with a sampling time of 64s at  $1.70\mu\text{m}$ . The bottom panel shows the X-ray counterpart to these flares with a sampling time of 300 sec. These X-ray flares are identified as flare #4 and #5 by Porquet et al. (2008). (b - Right) Similar to (a) except for a NIR and X-ray flare that occurred on April 2, 2007.

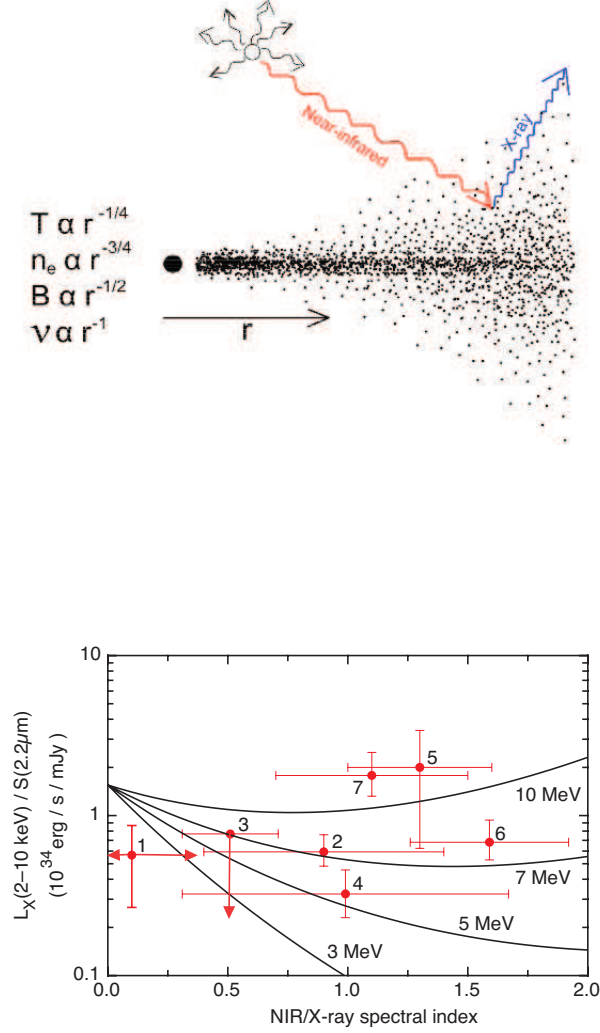


Fig. 22.—: (*a - top*) A schematic diagram of the ICS picture for Sgr A\*. The scaling relations to the left of the diagram show the variation of the magnetic field ( $B$ ), electron density ( $n_e$ ), the characteristic frequency ( $\nu$ ) of radio emission and the temperature ( $T$ ) of a quasi-spherical disk as a function of radius (Loeb & Waxman 2007). The size of flare emission is not scaled. (*b - bottom*) Solid curves show the ratio of inverse Compton X-ray luminosity (2–10 keV) to NIR synchrotron flux (at  $2.2\mu\text{m}$ ) as a function of NIR or X-ray spectral index  $\beta$  (where  $S_\nu \propto \nu^{-\beta}$  created by upscattering of optical/NIR photons from an electron population with radius  $R = 10 R_s$ , and uniform density  $n_e = 10^7 \text{ cm}^{-3}$ , and temperatures of 3, 5, 7, and 10 MeV. Points labeled 1 to 7 indicate the measured ratios and IR spectral indices of the seven X-ray flares with known NIR counterparts. (1) 2004 Jul 07, Eckart et al. (2006, X-ray: flare  $\phi_3$ , IR: flare III); (2) 2004 Aug 31, X-ray: Belanger et al. (2005), IR: Yusef-Zadeh et al. (2006); (3) 2006 Jul 17, X-ray: Marrone et al. (2008), IR: lower limit from Hornstein et al. (2007); (4) 2007 Apr 02, X-ray: Porquet et al. (2008, flare 1), IR: this paper (flare 2A); (5) 2007 Apr 04 05:25, X-ray: Porquet et al. (2008, flare 2), IR Dodds-Eden et al. (2009); (6) 2007 Apr 04 14:37, X-ray: Porquet et al. (2008, flare 4), IR: this paper (flare 4A); and (7) 2007 Apr 04 16:45, X-ray: Porquet et al. (2008, flare 5), IR: upper limit from this paper (flare 4B). Where the NIR spectral index is not known, the measured X-ray spectral index is used (points 2, 5 and 7); the NIR and X-ray spectral indices are both unknown for point 1. NIR measurements for points 2–7 are scaled to  $2.2\mu\text{m}$  using either the NIR or X-ray spectral index. The measured 2–8 keV X-ray luminosities for points 1 and 3 have been rescaled to 2–10 keV by multiplication by  $4/3$ .

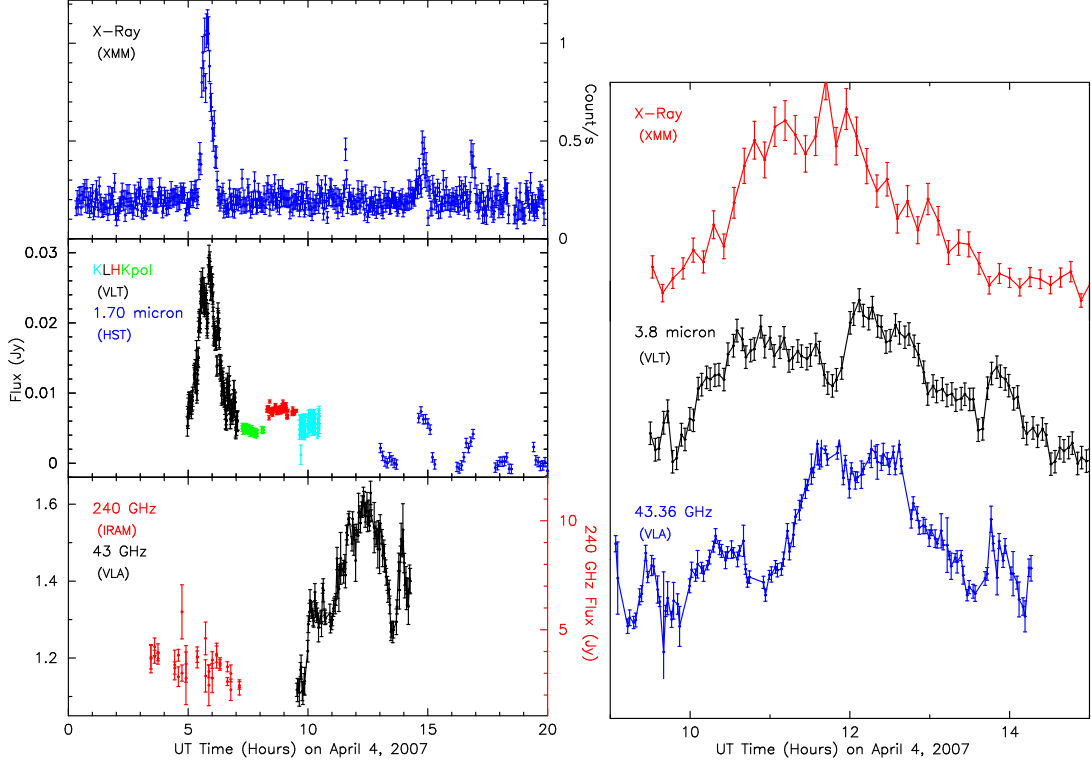


Fig. 23.—: (*a - Left*) The light curves of Sgr A\* on 2007, April 4 obtained with XMM in X-rays (top), VLT and HST in NIR (middle) and IRAM-30m and VLA at 240 GHz and 43 GHz, respectively (bottom). The NIR light curves in the middle panel are represented as H ( $1.66 \mu\text{m}$ ) in red,  $K_s$  and  $K_s$ -polarization mode ( $2.12 \mu\text{m}$ ) in green and light blue, respectively,  $L'$  ( $3.8 \mu\text{m}$ ) in black (Dodds-Eden et al. 2009), and NICMOS of HST in blue at  $1.70 \mu\text{m}$ . In the bottom panel, red and black colors represent the 240 and 43 GHz light curves, respectively. (*b - Right*) The top two plots show the light curves of Sgr A\* obtained with the XMM and VLT whereas the bottom panel shows the light curve taken with the VLA at 43 GHz. The X-ray and NIR light curves are shifted by 3.05 hours and stretched by a factor of 5.7. The 43 GHz light curve is baseline subtracted in order to remove the slope due to the quiescent component of Sgr A\*.

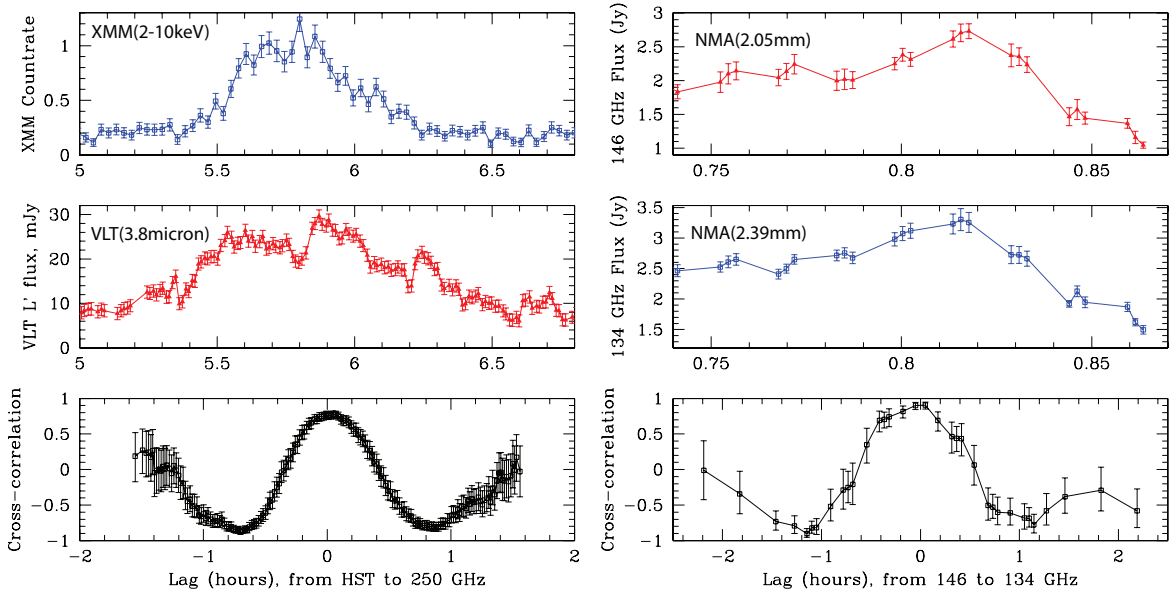


Fig. 24.—: (a - Left) The top and middle plots show the X-ray and NIR light curves taken on 2007, April 4. The cross correlation plot in the bottom panel indicates a peak at  $-0.5^{+7.0}_{-6.5}$  minutes time delay. (b - Right) The light curves shown in the top and center panels are measured simultaneously with the NMA at 146 GHz and 134 GHz on 2007, April 4, respectively. The cross correlation plot shows a peak with  $3^{+3.4}_{-8.0}$  minutes time delay. The time delays in both plots are consistent with zero.

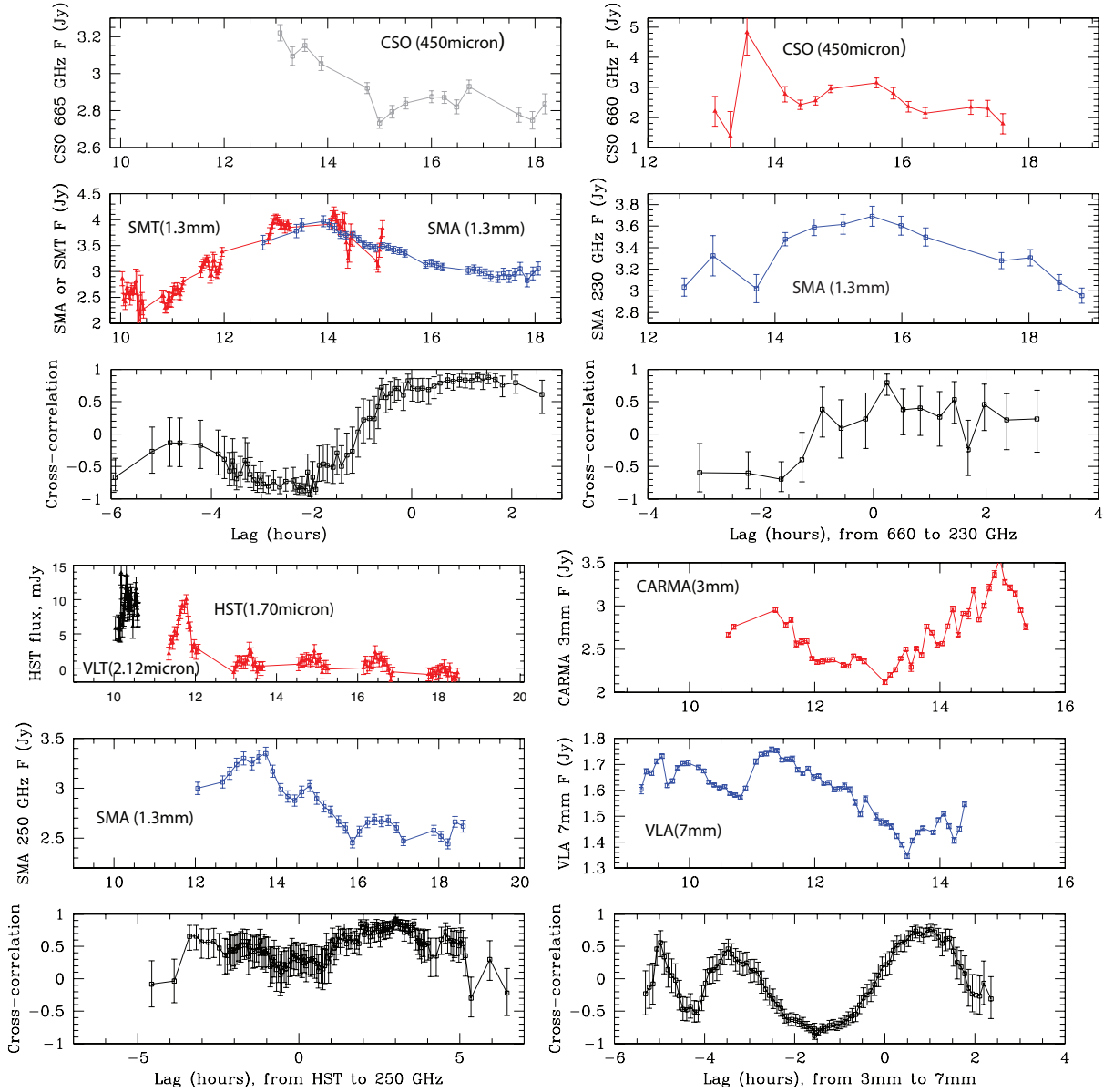


Fig. 25.—: (a - Top Left) The light curve of Sgr A\* at 450  $\mu\text{m}$  (665 GHz) is shown in the top panel whereas the 230 GHz (1.3mm) light curve in the middle panel is based on combining SMT and SMA observations on 2007, April 3 with UT ranges 10:07h - 14:56h and 12:44h - 18:3.8h. A constant offset due to the contamination of a steady background emission is subtracted from the SMT data. The bottom panel represents the cross correlation plot showing a peak with  $1.32^{+0.33}_{-0.63}$  hours time delay. (b - Top Right) Similar to (a) except that the light curves are taken on 2007, April 1 at 450  $\mu\text{m}$  and 230 GHz using the CSO and SMA, respectively. The peak of the cross correlation shows a  $0.24^{+1.12}_{-0.29}$  hours time delay. (c - Bottom Left) Similar to (a) except that NIR light curve is based on combining the data taken with the VLT and NICMOS whereas the 230 GHz data taken with the SMA on 2007, April 5. The cross correlation is constrained to have a peak of  $2.64^{+0.5}_{-0.67}$  hours time delay. (d - Bottom Right) The light curves shown in the top and center panels are based on CARMA and VLA observations at 94 GHz and 43 GHz on 2007, April 2, respectively. The cross correlation plot shows a peak with  $1.02^{+0.16}_{-0.31}$  hours of time delay. One  $\sigma$  error bars are given for all the time lags.

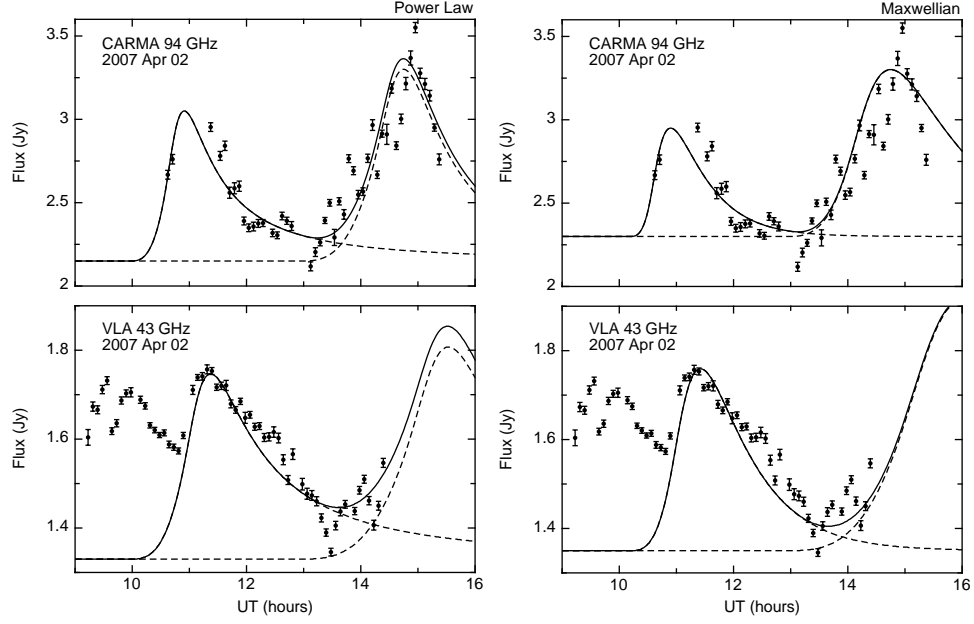


Fig. 26.—: (a - Left) A fit to the CARMA data at 94 GHz using two flares are shown in the top panel. The expanding blob model automatically generates the fit to the VLA data at 43 GHz, as shown in the bottom panel. The model has used a power law distribution of electrons. (b - Right) Similar to (a) except that a Maxwellian distribution of particles is used to fit simultaneously the CARMA and VLA light curves obtained on 2007 April 2.

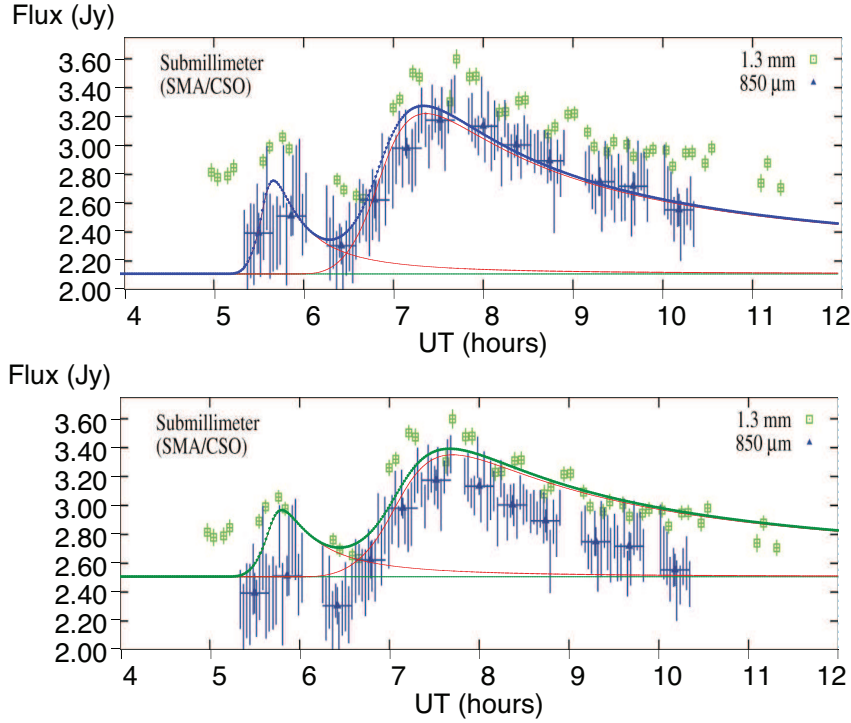


Fig. 27.—: The SMA and CSO data are taken on 2006 July 17 at 1.3mm and 850 $\mu\text{m}$ , respectively (Marrone et al. 2008). After background subtraction, the two weak and strong flares are fitted simultaneously, supporting the plasmon model. The expanding blob model automatically generates the fit to the 850 $\mu\text{m}$  data (top panel) in blue and to the 1.3mm data (bottom panel) in green.